Bulletin of Earthquake Engineering
https://doi.org/10.1007/s10518-025-02315-6

ORIGINAL ARTICLE

Ground motion models for Campi Flegrei (Italy)

Antonio Scala[1,3] · Claudio Strumia[1] · Pasquale Cito[2] · Francesco Scotto di Uccio[1] · Gaetano Festa[1,4] · Iunio Iervolino[2,5] · Aldo Zollo[1] · Antonella Bobbio[3] · Vincenzo Convertito[3] · Luca Elia[1,3] · Antonio Emolo[1] · Antonio Giovanni Iaccarino[1]

Received: 5 January 2025 / Accepted: 5 November 2025

Abstract
Ground Motion Models (GMMs) are empirically-calibrated equations relating ground motion intensity measures to earthquake magnitude, source-to-site distance, geological local site conditions, and possibly other covariates. GMMs are employed for applications such as probabilistic seismic hazard analysis and post-event rapid shaking estimation. Since early 2014, the densely populated Campi Flegrei caldera in Southern Italy has experienced increasing seismicity, concomitant to the volcanic unrest and ground uplift, with over ten thousand recorded events, with duration magnitude larger than -1.1. In the period between March 2022 and May 2024, seismic activity has intensified, including approximately seventy events with duration magnitudes between 2.5 and 4.4, most of them widely felt, in some cases causing non-negligible seismic structural actions close to the source, and ultimately sparking large public concern. In this study, we calibrated site-specific GMMs for peak ground acceleration, peak ground velocity, and 5% damped spectral pseudo-acceleration for 18 vibration periods T ranging from $0.02\,s$ to $5\,s$. The dataset includes recordings from the events with duration magnitude greater than or equal to 2.5 over the period 03/22 − 05/24 recorded by more than 50 accelerometric and velocimetric seismic stations at epicentral distances $R_{epi} < 40\,km$. Moment magnitude, which is the scale used in the GMMs, was derived for the events from their displacement Fourier amplitude spectrum. The GMMs show larger spectral amplitudes at short periods($T < 0.4\,s$), and faster attenuation with distance ($R_{epi} \geq 5km$) as compared to some existing ground motion models for Italy.

Keywords Ground motion prediction equations · Volcano earthquakes · Seismic hazard · Seismic risk · Campi flegrei

1 Introduction

Ground Motion Models (GMMs), are semi-empirical relationships commonly used to predict ground motion intensity measures (IMs), such as peak ground velocity (PGV), peak ground acceleration (PGA) and spectral pseudo-acceleration (referred to as SA) at different

Extended author information available on the last page of the article

Published online: 19 November 2025

natural vibration periods T, for a given viscous damping factor. They relate the logarithm of the IM at a site of interest to earthquake parameters, such as source-to-site distance, magnitude, proxies for local waves propagation (i.e., so-called *site effects*), and possibly other covariates, such as faulting style. GMMs are key models for seismological and earthquake engineering applications, such as probabilistic seismic hazard analysis or PSHA (McGuire 2004) and rapid post-event shaking estimation for emergency management. As an example, the ShakeMap (v4.0) tool (Wald et al. 1999) in Italy, implemented by *Istituto Nazionale of Geofisica e Vulcanologia* (INGV), provides maps of the shaking (PGA, PGV, SA and macroseismic intensity in terms of the Mercalli-Cancani-Sieberg scale), in the area struck by an earthquake with magnitude equal to or larger than 3.0, based on GMM predictions conditional to IM observations as detected by seismic monitoring in addition to earthquake magnitude and location. Most of the largest earthquakes in Italy occur in tectonic areas (e.g., 2009 L'Aquila earthquake, Chiaraluce et al. 2011; and 2016–2017 Central Italy sequence, Michele et al. 2020). Nevertheless, seismic activity of different origin also characterizes the Italian volcanic areas, such as at Mt. Etna (Scarfì et al. 2023), Mt. Vesuvius (Ricco et al. 2021), Aeolian Islands (Di Luccio et al. 2021), Ischia Island (Selva et al. 2021) and Campi Flegrei. In these areas, seismic sequences are considered to be driven by several phenomena such as fluid (magma, gas) migration to the surface (Lanzano and Luzi 2020), or by the evolution of the hydrothermal activity generating abrupt changes in the shallow crust stress conditions (Giudicepietro et al. 2021; Keir et al. 2021). Despite being generally characterized by magnitudes considered small-to-moderate otherwise, these earthquakes sometimes lead to concern close to their epicenters, also due to their relative shallow hypocentral depth and the relatively high urbanization of some of these areas.

GMMs calibrated using moderate-to-large magnitude events in areas where deformation is primarily of tectonic origin (e.g., Bindi et al. 2011) have been found to be not generally applicable to volcanic areas, where shallower locations and faster attenuation with distance are generally observed (Ramadan et al. 2023). Consequently, some GMMs have been calibrated ad-hoc in Italy. Tusa and Langer (2016), Peruzza et al. (2017) and Tusa et al. (2020) proposed models based on data recorded in the Mt. Etna volcanic area, while Lanzano and Luzi (2020) and Ramadan et al. (2023) proposed the updated GMMs including data from the Aeolian and Ischia islands and a single earthquake from Campi Flegrei. However, the different Italian volcanic areas are characterized by considerably different geomorphological settings including high volcanic cones (like Mt. Etna and Mt. Vesuvius) with prevalence of rock sites, volcanic islands (Ischia and Aeolian islands) and calderas (Campi Flegrei), with the latter two being apparently characterized mainly by stiff and soft soils. Therefore, the exportability of each of these models outside the region for which they were calibrated can be questioned.

Campi Flegrei is a caldera bordering Naples, one of the largest cities in Italy. During its geological history, the area has experienced cyclical processes of subsidence and uplifts (Gaeta et al. 2003; Del Gaudio et al. 2010; D'Auria et al. 2011; Bevilacqua et al. 2022). Seismic activity often accompanies ground deformation, with the intensity and rate of seismic events correlating with uplift rates (Bevilacqua et al. 2022, 2024; Tramelli et al. 2022). Between March 2022 and May 2024, uplift rates reached peaks of 2 cm/month, and about 9,000 earthquakes with a duration magnitude (M_d) above -1.1 were recorded from 2014 to May, 2024 (Scotto di Uccio et al., 2024), including three earthquakes with $M_d \geq 4.0$. Some of the strongest events subjected structures – at least those featuring a very short fun-

damental vibration period and located particularly close to the source of the event – to seismic forces exceeding those prescribed by the current building code for seismic design in the area as recently shown by Iervolino et al. (2024), where a preliminary version of these GMMs were presented (yielding similar results as those presented herein).

In Italy, the design seismic actions stem from the PSHA study of Stucchi et al. (2011), in which the model of De Natale et al. (1988) is also used for ground motion propagation modelling in volcanic areas, while the ShakeMap developed by INGV for such areas makes use of the GMMs proposed by Tusa and Langer (2016). Thus, considering the large amount of recent data, we here calibrate local (i.e., regional) GMMs for Campi Flegrei. The targeted IMs are the PGA, PGV and 5% damped SAs at vibration periods in the range $[0.02s,\ 5s]$. These IMs are intended as the horizontal maxima (i.e., the largest between the two horizontal components) and the vertical component. The model applies for events with moment magnitude (M_w) in the range 1.5-4.0 (corresponding to duration magnitude M_d range 2.5–4.4, see Sect. 2.2) and for epicentral distance up to $40\ km$.

The paper is structured as follows. In Sect. 2 the used dataset is described, in Sect. 3 the GMMs calibration is presented and the proposed GMMs are used to map the estimated ground shaking, in terms of some IMs, in the case of the $M_d = 4.4$ $(M_w = 4.0)$ event occurred on 20 May 2024. Then, a deeper discussion of the results and some final remarks are provided in Sects. 4 and 5, respectively.

2 Dataset

2.1 Event waveforms and locations

Between 1st January 2016 and 21st May 2024, the ONT (*Osservatorio Nazionale Terremoti*, Italian national earthquake observatory https://terremoti.ingv.it) reported 1127 events with M_d in the range [0.3,4.4] recorded in the area of the Campi Flegrei caldera, according to the location computed by the *Osservatorio Vesuviano* section of the INGV (INGV-OV, https://terremoti.ov.ingv.it/gossip/flegrei/index.html, Ricciolino et al. 2024). A refined catalogue was obtained, locating about 9,000 events from 2014 to 2024, with a minimum duration magnitude $M_d = -1.1$ (Scotto di Uccio et al. 2024). From these catalogues, 71 earthquakes with $M_d \geq 2.5$ had been recorded since March 2022 to May 2024.

For the selected events, where available, we used the location computed by Scotto di Uccio et al. (2024), which relocated the events in the Campi Flegrei area until 13th April 2024, constraining hypocentral locations integrating source-specific station corrections and waveforms coherency. The achieved resolution in the mentioned catalogue, whose uncertainties in hypocentral location are in the order of 100 m, contributed to illuminate causative geological structures in the area. For the remaining earthquakes, we used the location provided by the INGV-OV bulletin. The complete catalogue and the subset used for the calibration of GMM parameters are available in the repository by Scala (2025).

2.2 Moment magnitude

The reference catalogue for the Campi Flegrei caldera, as released by the INGV, characterizes the seismicity in terms of M_d. Nevertheless, for consistency with GMMs used for

seismic hazard-related analyses, we estimated M_w (Kanamori 1977; Hanks and Kanamori 1979) for the 71 $M_d \geq 2.5$ events in the dataset recorded from March 2022 to May 2024. This selection ensured a consistent magnitude range with the one in Ramadan et al. (2023), although centred at lower magnitudes. We estimated M_w from the inversion of S-wave displacement spectra using the non-linear probabilistic method of Supino et al. (2019). Such an inversion strategy grounds on the generalized source description proposed by Brune (1970) and Boatwright (1980) through three source parameters: the seismic moment, M_0, the corner frequency, f_c, and the decay exponent. In the propagation, we considered a body-wave geometrical spreading and a constant quality factor (Q) (Supino et al. 2019).

The spectra were evaluated by selecting traces recorded within about $20\,km$ from the epicentres, and extracting $3\,s$ time windows around the S-pick (from S-waves picking), starting $0.15\,s$ before the pick, to account for possible uncertainties in the phase identification. An average density $\rho = 2.5\,g/cm^3$ (Judenherc and Zollo 2004) was used for describing the propagation medium in the area, while the 1D velocity model proposed by Tramelli et al. (2022) was linearly interpolated to model the low frequency amplitude level of the spectra for each event, attributing S-wave velocity according to the hypocentral depth. The Q_S factor (quality factor for S-waves) was inferred for each station-event pair by minimizing the misfit with the observations, while systematically exploring values in the range $Q_S \in [30,\ 200]$, representative for the area of interest (Calò and Tramelli 2018).

For each event, M_0 was inferred from the low-frequency plateau level of the displacement spectra observed at individual stations. When analyzing the single station estimates of the seismic moment as a function of the hypocentral distance (see Figure S1a in Supplementary Material), we found a dependance that deviates from the geometrical spreading, suggesting a stronger attenuation contribution moving away from the seismic sources. This effect may be ascribed to the medium heterogeneity and complex anelastic attenuation, not completely modeled by a frequency independent Q_S factor. To minimize potential errors in estimating M_w, we introduced a station-specific correction. This involves the analysis of the differences (residuals) between the seismic moment estimates for individual stations and the event average, grouping these residuals by distance (Figure S1b in Supplementary Material). From this, we calculated an average correction for the seismic moment within each distance range. This correction was then applied to single station M_w estimates in each distance range, and the weighted mean of M_w among the stations was used as estimate for each event. Following this strategy, we retained 67 out of the 71 events, as shown in Fig. 1(a). One event was discarded due to the low signal-to-noise ratio, while other three events were discarded since the waveform processing (see Sect. 2.3) failed to provide trustable ground motion peak parameters. Within the zoomed inset of Fig. 1(a), the size of the epicentres scales with the earthquake magnitude, highlighting that the largest events occurred at larger depths.

For the calibration of the GMMs, we initially considered waveforms recorded by 99 stations within an epicentral distance $R_{epi} < 100\,km$. However, from preliminary analysis, we noticed that the GMMs predicted, at 95% level of confidence and at $R_{epi} > 40\,km$, very low amplitudes of shaking for the larger modelled magnitude, that is PGA $< 0.06\,cm/s^2$, and SA $(T = 0.3\,s) < 0.2\,cm/s^2$. Thus, we limited the calibration to data recorded at the 52 stations within $40\,km$ in terms of epicentral distance. Nevertheless, all intensity data within the $40 - 100\,km$ range have been made available in Scala (2025), providing a valuable resource for future efforts, aimed at refining volcanic GMMs on a national scale.

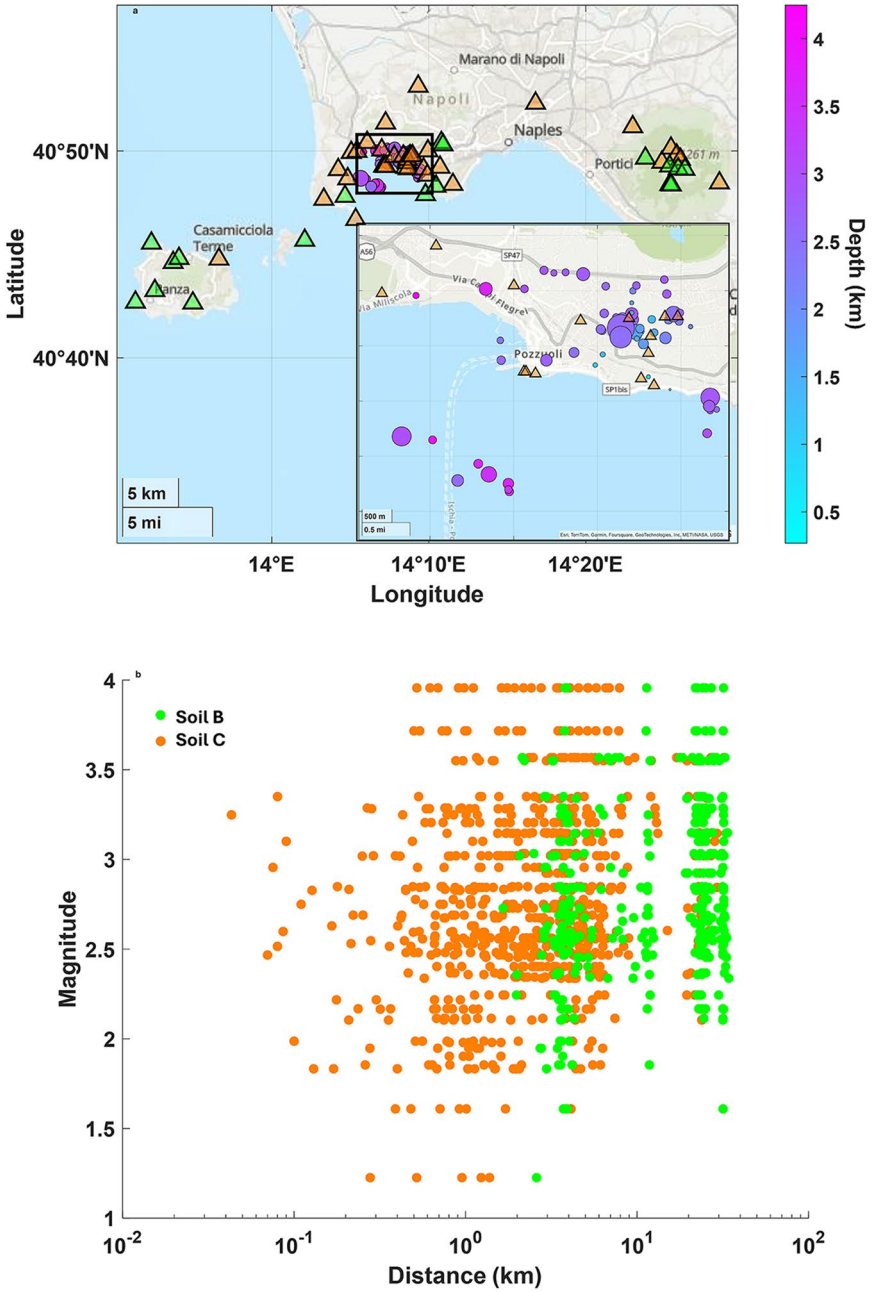

Fig. 1 (**a**) Epicentres distribution of the selected events along with the seismic stations. The depth of the events is marked through the right-sided colour scale while green and orange triangles represent stations on sites B and C according to the EC8 classification, respectively. In the inset of panel (**a**) a zoom around the epicentres of the events with size of circles scaling with M_w is shown. (**b**) Epicentral distance and moment magnitude of the records with the EC8 classification of data highlighted using the same colour scale adopted for the stations in panel (**a**)

Among the used 52 stations, 35 are owned by the Italian National Seismic Network (INSN, code IV) managed by INGV-OV, NAPI belongs to the *Irpinia Seismic Network* (ISNet, code IX) operated by the *University of Naples Federico II*, while the remaining 16 stations are part of the national accelerometric network managed by the Italian Department of Civil Protection (*Rete Accelerometrica Nazionale*, *RAN*, code IT). NAPI and all the RAN stations are equipped with an accelerometer while 14 out of the 35 stations of IV network are equipped only with velocimeter. For the remaining stations, equipped with both an accelerometer and a velocimeter, after a preliminary consistency check, we processed both the accelerometric and velocimetric data to extract ground motion parameters. If both records passed the quality check (described below in Sect. 2.4), the accelerometric data are selected. The list of the stations including the general features of the sensors is provided in Scala (2025), where it is also reported whether the velocimeter is a broadband sensor.

2.3 Site effects

Several models were recently proposed as proxies for local site effects within GMMs, leveraging surface geology and shear wave shallow velocity (e.g., Forte et al. 2019). Here, we used the Italian shear wave shallow velocity in the upper 30 m of soil, V_{s30}, map, and the related soil classification in terms of the Eurocode 8 categories (EC8, CEN 2004), proposed by Michelini et al. (2019), according to the standard classification of the Italian ShakeMap. Thus, 19 sites are classified as stiff soils (EC8 code B, $360\,m/s \leq V_{s,30} < 800\,m/s$) while the remaining 33, including all the ones located within the inner caldera, as soft soils (EC8 code C, $180\,m/s \leq V_{s,30} < 360\,m/s$). The stations used in this work are plotted in Fig. 1(a) highlighting the separation between soil classification. The classification is also given, for each station, in Scala (2025).

2.4 Data processing

The whole dataset was uniformly processed through the software GMProcess developed by the *United States Geological Survey* (USGS) (https://ghsc.code-pages.usgs.gov/esi/groundmotion-processing/, last accessed May 2024). Before removing the instrumental response, a band pass filter with corner frequencies at 0.005 Hz and 0.9 times the Nyquist frequency, and a water level to 60 dB were applied (see GMProcess manual about signal processing at https://ghsc.code-pages.usgs.gov/esi/groundmotion-processing/contents/manual/processing.html). The ground motion parameters were extracted for the signals reporting a signal-to-noise-ratio larger than 2 in the whole frequency band between 0.5 Hz and 7.5 Hz. This choice represented a compromise for the sampled magnitude range since more than 95% of the events feature f_c values within this range, with about 85% of them having $f_c < 3.75\,Hz$. Similarly to previously proposed GMMs for Italian volcanic regions (Ramadan et al. 2023), we extended the period range for SA regressions from $0.02\,s$ to $5.0\,s$. For the proposed GMMs, this was particularly relevant at high frequency, since several recordings exhibited notable peaks in the response spectra at short periods (generally below 0.3 s). The final dataset consisted of 1207 records, for which the PGA, PGV and SA were computed. As previously defined, the horizontal IMs were defined as the largest between the two components.

Figure 1(b) shows the moment magnitude vs. epicentral distance distribution of the records with colours highlighting the soil classification. The two different soil types are

uniformly distributed at all magnitudes and distances range, except at very short distances (i.e., within the inner caldera area) where the classification available only reports soft soil.

PGA is plotted as a function of distance and magnitude in Figure S2 in Supplementary Material for both M_d and M_w. This comparison suggests how the use of the moment magnitude leads to a less scattered and more consistent attenuation behaviour.

3 Results

3.1 GMM calibration

Recently, several GMMs for Italian volcanic areas have been proposed (e.g. Tusa and Langer 2016; Tusa et al. 2020; Lanzano and Luzi 2020; Ramadan et al. 2023). Among these models, Tusa and Langer (2016; hereinafter TL16) is the only one using the epicentral distance as covariate and it is calibrated using seismic data from the Etna volcano in Sicily. This model is currently adopted for the computation of the ShakeMap released by INGV when earthquakes in Italian volcanic areas occur (https://shakemap.ingv.it/archive.html), including Campi Flegrei. The more recent model of Ramadan et al., 2023 (hereinafter RLS23) is based on hypocentral distance (R_{hypo}) and integrates data from Etna with earthquakes occurred close to Aeolian islands, the 2017 Ischia earthquake and one event occurred in Campi Flegrei in 2022. Both GMMs propose different attenuation models for shallow and deep events imposing a focal depth of $5\ km$ to separate the two different cases. Among the dataset of events considered within this work, no earthquakes were located at depths larger than $5\ km$ ($z_{max}\ = 4.2\ km$) and hence we calibrated a single-depth ground motion model.

The TL16 and RLS23 models propose the following functional form for shallow events:

$$\begin{cases} \log_{10} IM = a + b\cdot\ M + c\cdot \log_{10}\sqrt{R_{epi}^2 + h^2} + e_i\cdot\ S_i + \varepsilon \\ \log_{10} IM = a + b\cdot\ M + [c + c_2\cdot\ (M - 4.8)]\cdot \log_{10}\sqrt{R_{hypo}^2 + h^2} + e_i\cdot\ S_i + \varepsilon \end{cases} \quad (1)$$

In the Eq. (1), IM is the considered ground motion intensity measure, a is the intercept, while b and c represent the coefficients controlling the dependence on magnitude M and geometrical attenuation with distance, respectively. c_2 is the coefficient accounting for a magnitude dependent geometrical attenuation. The term h is an average pseudo-depth for TL16 and a fixed offset for RLS23, while the terms $e_i\cdot\ S_i$ are used to account for the different site amplifications through the dummy variable S_i that take the values 1 or 0 depending on whether the observation was recorded on that specific site condition or not. For both TL16 and RLS23, the term e_A, indicating rock site conditions, is equal to 0, and the other terms represent the amplification due to the sites B, C, D and E, respectively. Finally, ε is the residual term. In the case of TL16, this latter is divided into between-event ($\delta\ B_e$) and within-event residuals ($\delta\ W_{es}$), that is, $\varepsilon\ = \delta\ B_e + \delta\ W_{es}$. In the case of RLS23, the within-event residual is further divided into site-to-site ($\delta\ S2S_s$) and a remaining residual (ϵ), that is $\varepsilon\ = \delta\ B_e + \delta\ S2S_s + \epsilon$ (e.g., Al-Atik et al. 2010). In both cases ε is a normal random variable with zero mean and σ_T standard deviation. It follows that IM is a lognormal random variable conditional to magnitude, distance and soil condition, whose mean will

be indicated as $\overline{\log_{10}(IM)}$ in hereafter. Assuming that the components of the total residual are stochastically independent random variables, the standard deviation σ_T, for the two models shown in Eq. (1), assumes the following shapes:

$$\begin{cases} \sigma_T = \sqrt{\tau^2 + \varphi^2} \ (TL16) \\ \sigma_T = \sqrt{\tau^2 + \phi_{S2S}^2 + \sigma_0^2} \ (RLS23) \end{cases} \tag{2}$$

with τ, φ, ϕ_{S2S} and σ_0 being the standard deviation of δB_e, δW_{es} $\delta S2S_s$ and ϵ, respectively.

As a preliminary analysis, we verified to what extent the previous GMMs fit the observed dataset recorded at Campi Flegrei as a function of distance. Figure 2 shows the boxplots of the distribution of the observed residuals computed as $\varepsilon = \log_{10}(Obs) - \overline{\log_{10}(IM)}$ with Obs referring to the observed PGA (panels a and c) and PGV (panels b and d). The predic-

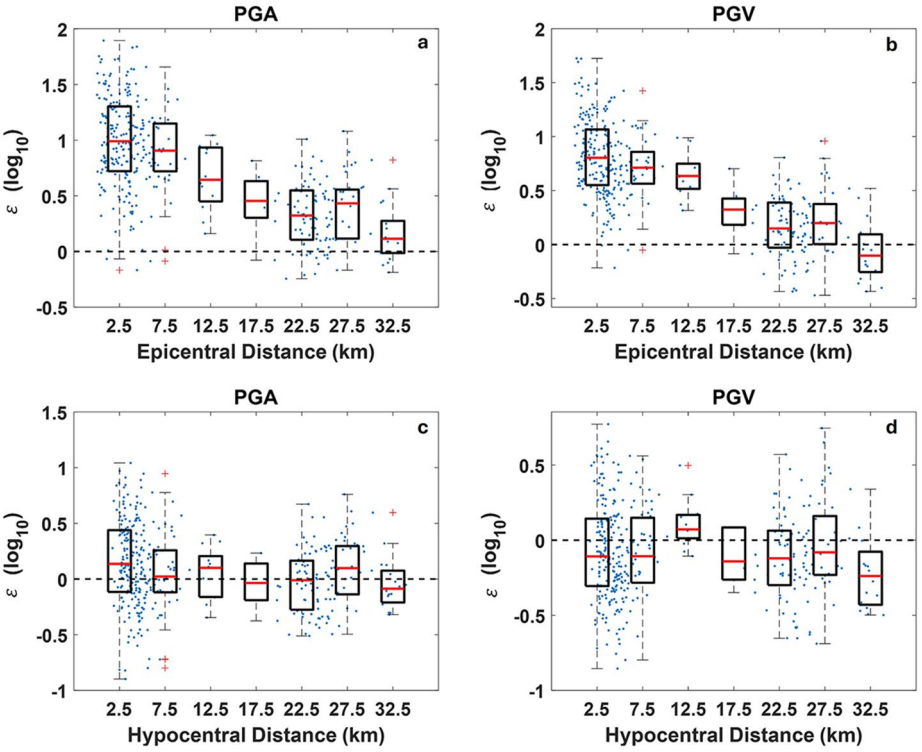

Fig. 2 Residuals (blue dots) and boxplots of observed shaking parameters as compared to the predicted values from available models. In each box the horizontal red line represents the median, the boxes contain values between 25th and 75th percentiles within each bin, while the red crosses mark the outliers, that are more than 1.5 times the interquartile range away from the bottom or top of the box. (**a**) ε for PGA as a function of the epicentral distance with prediction from TL16 GMM. (**b**) ε for PGV as a function of the epicentral distance with prediction from TL16 GMM. (**c**) ε for PGA as a function of the hypocentral distance with prediction from RLS23 GMM. (**d**) ε for PGV as a function of the hypocentral distance with prediction from RLS23 GMM

tion $\overline{\log_{10}(IM)}$ is based on TL16 (panels a and b) and RLS23 (panels c and d) GMMs. We considered either epicentral or hypocentral distances in top and bottom panels of Fig. 2, respectively, depending on the covariate used in the reference GMM. The TL16 model seems to underestimate the large values of the shaking observed at very short distances from the considered dataset. Conversely, at larger distances, the discrepancy between observed and predicted peaks is significantly reduced. Residuals for SA at vibration periods of interest to earthquake engineering, such as $0.3\ s$ and $1\ s$, exhibit similar trends, as shown in Figure S3 (panels a and b) in Supplementary Material. The underestimation is significantly reduced when using the RLS23 model and only affects the PGA at very short distances (Fig. 2c). On the other hand, a slight overestimation is observed for PGV (Fig. 2d) and SA (Figure S3 c and d in Supplementary material). It is worth highlighting that the shown biases are due to the specific features of the used dataset, which, for the first time, allows for the calibration of a GMM using a significant amount of data at very small distance ($R_{hypo} < 10\ km$). It should also be mentioned that the residual comparison includes only data from events with $M_w \geq 3.0$ consistently with applicability limits of the available models. Moreover, the geometrical mean and the maximum among horizontal components are used for comparison with TL16 and RLS23 in line with the observables adopted in those GMMs.

To establish the best functional form to calibrate a local GMM, we performed a set of *Bayesian Information Criterion* (BIC) tests. Such tests ground on the BIC parameter, which is defined as:

$$BIC = k \cdot \log_e(n) - 2 \cdot \log_e(L) \tag{3}$$

with k, n and L being the number of coefficients used to calibrate in the GMM, the number of data and the likelihood value, respectively. In this frame, the smaller BIC the better the model.

To perform the BIC tests let us consider the following functional form similar to the one proposed by RLS23 for shallow earthquakes:

$$\log_{10} IM = a + b \cdot M_w + (c + c_2 \cdot M_w) \cdot \log_{10} \sqrt{R^2 + h^2} + e_i \cdot S_i + \delta B_e + \delta S2 S_s + \epsilon \tag{4}$$

with R being either epicentral or hypocentral distance, (in km) and IM is given in cm/s^2 for PGA and SA and in cm/s for PGV.

For all the performed BIC tests, as well as for the final calibration of the GMM models, 65 out of the 67 events and 1145 records were used considering M_w estimated as described in Sect. 2.2. The remaining two events (IDs 38206821 and 38762741, M_w 3.2 and 2.8, respectively, see reference catalogue in Scala 2025) will be subsequently used to test the calibrated GMMs through a statistical analysis of the residuals. The regressions were performed using a linear mixed-effects regression, using the MATHWORKS-MATLAB function *fitlme* (academic License 40500131, last accessed August 2025) belonging to the *Machine Learning and Statistics Toolbox*, which estimates linear mixed-effects (LME) models via maximum likelihood methods (more details can be found on the documentation available at https://it.mathworks.com/help/stats/fitlme.html). The parameter h is imposed to be a fixed positive coefficient similarly to what shown in Lanzano and Luzi (2020) and Ramadan et al. (2023; RLS23),

The initial BIC tests were performed to determine the optimal value of parameter h for both epicentral and hypocentral distances. Figure S4(a) in Supplementary Material presents the BIC values for PGA using the epicentral and hypocentral distances as covariates, evaluated across different values of h. The results indicated that the optimal h is $1.4\,km$ for R_{epi} and $1.0\,km$ for R_{hypo}. Overall, the use of epicentral distance provided smaller BIC values and hence a better fit for PGA. For this reason, we selected epicentral distance as the covariate and set $h = 1.4\,km$.

In the second test, we compared the solution for the model shown in Eq. (4) (based on epicentral distance) with functional forms obtained adding either a term $b_2 \cdot M_w^2$ (accounting for a high order magnitude dependency) or a term $c_3 \cdot \sqrt{R_{epi}^2 + h^2}$ (accounting for anelastic attenuation). The results are summarized in Figure S4(b) in the Supplementary Material. The addition of these terms did not lead to a significant decreasing of the BIC parameter, for all the investigated IMs. Furthermore, the hypothesis tests for coefficients b_2 and c_3 being equal to zero exhibit relatively large $p-$values $(p > 0.05)$, particularly for PGA, PGV and short period SAs, suggesting that they do not have a statistically meaningful influence on IM (Wasserstein and Lazar 2016). In particular, regarding anelastic attenuation, the lack of significance of the c_3 coefficient may be attributed to the limited range of epicentral distances considered (i.e., $R_{epi} < 40\,km$). Indeed, it was highlighted how such term is primarily constrained by data at distance greater than $50\,km$ or become necessary when deeper events are accounted (e.g., Lanzano et al. 2019; Ramadan et al. 2023).

Finally, these tests suggested the use of the following R_{epi}-based functional form, incorporating a magnitude dependent geometrical attenuation:

$$\log_{10} IM = a + b \cdot M_w + (c + c_2 \cdot M_w) \log_{10} \sqrt{R_{epi}^2 + h^2} + e_c \cdot S_c + \delta B_e + \delta S2S_s + \epsilon \quad (5)$$

with a, b, c, c_2 and e_c representing the fixed effect and e_c controlling the amplification of soil C with respect to soil B. $h = 1.4\,km$ is a fixed coefficient, while δB_e, and $\delta S2S_s$ are the mixed-effects obtained grouping data by events and stations respectively with ϵ being the remaining residual.

A similar calibration, based on hypocentral distance (setting $h = 1.0\,km$) will be presented in the discussion section (Sect. 4.1).

The coefficients for the GMMs calibrated using the functional form of Eq. (5) are listed in Table 1, along with the standard errors and the p-values. In Table 1, τ, ϕ_{S2S}, σ_0, σ_T (see Eq. 2) are also reported. The between-event and the delta site-to-site residuals, for PGA, are included in the data repository (Scala 2025) associated with the corresponding event and site in the catalogue and station description, respectively. It is worth noting that all the residuals τ, ϕ_{S2S}, σ_0 are directly estimated by the implemented algorithm as described in the function documentation (https://it.mathworks.com/help/stats/fitlme.html) and not as the standard deviation of the residuals distribution in order to avoid underestimation (Campbell et al. 2025; Kuehn et al. 2025).

The calibrated GMMs are also shown for PGA (Fig. 3a) and PGV (Fig. 3b), for four different magnitude values ($M_w = 2.5,\ 3.0,\ 3.5,\ 4.0$), highlighting the different prediction for soils C and B. Similarly, GMMs for SAs at the periods $T = 0.05\,s,\ 0.3\,s,\ 1.0\,s$ and $1.5\,s$ are shown in Fig. 3(c), 3(d), 3(e) and 3(f), respectively. The parameter e_c shows that

Table 1 Coefficients of horizontal GMMs calibration (maximum among horizontal components) for PGA, PGV and SAs with the functional form of Eq. (5). Parameter h = 1.4 km for all the IMs

Parameters	a	b	c	c_2	e_c	τ	ϕ_{S2S}	σ_0	σ_T
PGA	0.4094	0.6191	-3.6229	0.3639	0.1493	0.1746	0.2260	0.2496	0.3793
SE	0.1627	0.0518	0.1258	0.0398	0.0746				
p-value	0.0120	0.0000	0.0000	0.0000	0.0458				
PGV	-1.6914	0.7191	-3.0713	0.3046	0.0888	0.1749	0.2150	0.2023	0.3431
SE	0.1516	0.0490	0.1037	0.0325	0.0692				
p-value	0.0000	0.0000	0.0000	0.0000	0.1994				
SA 0.02 s	0.6010	0.5958	-3.8461	0.4186	0.1392	0.1859	0.2304	0.2835	0.4099
SE	0.1759	0.0564	0.1415	0.0451	0.0776				
p-value	0.0007	0.0000	0.0000	0.0000	0.0733				
SA 0.03 s	0.7359	0.5996	-3.9841	0.4293	0.1883	0.2007	0.2436	0.2972	0.4336
SE	0.1874	0.0603	0.1485	0.0473	0.0820				
p-value	0.0001	0.0000	0.0000	0.0000	0.0218				
SA 0.05 s	0.8067	0.6108	-3.9975	0.4276	0.2107	0.1968	0.2346	0.2959	0.4258
SE	0.1842	0.0594	0.1474	0.0470	0.0795				
p-value	0.0000	0.0000	0.0000	0.0000	0.0081				
SA 0.075 s	0.6920	0.6134	-3.7435	0.3984	0.2275	0.1926	0.2313	0.2753	0.4079
SE	0.1774	0.0572	0.1380	0.0439	0.0775				
p-value	0.0001	0.0000	0.0000	0.0000	0.0034				
SA 0.1 s	0.5311	0.6229	-3.3363	0.3146	0.2256	0.1908	0.2447	0.2466	0.3964
SE	0.1719	0.0550	0.1255	0.0395	0.0796				
p-value	0.0021	0.0000	0.0000	0.0000	0.0047				
SA 0.15 s	0.1077	0.6844	-2.7511	0.2056	0.2316	0.1732	0.2328	0.2158	0.3616
SE	0.1555	0.0495	0.1105	0.0346	0.0747				
p-value	0.4886	0.0000	0.0000	0.0000	0.0020				
SA 0.2 s	-0.1031	0.6885	-2.6100	0.2187	0.2120	0.1716	0.2370	0.2006	0.3548
SE	0.1520	0.0483	0.1035	0.0322	0.0751				
p-value	0.4977	0.0000	0.0000	0.0000	0.0048				
SA 0.25 s	-0.3742	0.7479	-2.4484	0.1875	0.1707	0.1819	0.2409	0.1918	0.3576
SE	0.1557	0.0500	0.0995	0.0309	0.0757				
p-value	0.0164	0.0000	0.0000	0.0000	0.0243				
SA 0.3 s	-0.5983	0.7810	-2.3072	0.1662	0.1514	0.1870	0.2529	0.1830	0.3639
SE	0.1578	0.0507	0.0956	0.0295	0.0785				
p-value	0.0002	0.0000	0.0000	0.0000	0.0541				
SA 0.4 s	-0.9019	0.8098	-2.2243	0.1734	0.1213	0.1940	0.2573	0.1709	0.3648
SE	0.1597	0.0517	0.0898	0.0276	0.0792				
p-value	0.0000	0.0000	0.0000	0.0000	0.1258				
SA 0.5 s	-1.2458	0.8286	-2.0745	0.1769	0.1561	0.2139	0.2585	0.1627	0.3729
SE	0.1691	0.0559	0.0859	0.0264	0.0791				
p-value	0.0000	0.0000	0.0000	0.0000	0.0488				
SA 0.75 s	-1.6757	0.8439	-2.1797	0.2413	0.1589	0.2251	0.2283	0.1621	0.3592
SE	0.1727	0.0585	0.0851	0.0263	0.0707				
p-value	0.0000	0.0000	0.0000	0.0000	0.0249				
SA 1.0 s	-1.9719	0.8556	-2.3701	0.3094	0.1575	0.2329	0.2254	0.1702	0.3660
SE	0.1781	0.0606	0.0890	0.0276	0.0704				
p-value	0.0000	0.0000	0.0000	0.0000	0.0254				
SA 1.5 s	-2.3896	0.8644	-2.6398	0.3780	0.2010	0.2425	0.2092	0.1781	0.3664
SE	0.1836	0.0631	0.0925	0.0288	0.0663				

Table 1 (continued)

Parameters	a	b	c	c_2	e_c	τ	ϕ_{S2S}	σ_0	σ_T
p-value	0.0000	0.0000	0.0000	0.0000	0.0025				
SA 2.0 s	-2.6768	0.8664	-2.7034	0.3972	0.2272	0.2509	0.2030	0.1844	0.3717
SE	0.1890	0.0653	0.0954	0.0298	0.0650				
p-value	0.0000	0.0000	0.0000	0.0000	0.0005				
SA 3.0 s	-2.7556	0.8177	-3.0000	0.4472	0.1923	0.2360	0.1757	0.1917	0.3512
SE	0.1794	0.0622	0.0978	0.0309	0.0579				
p-value	0.0000	0.0000	0.0000	0.0000	0.0009				
SA 4.0 s	-2.7906	0.7817	-3.1544	0.4670	0.1771	0.2207	0.1724	0.1965	0.3421
SE	0.1711	0.0589	0.0998	0.0316	0.0573				
p-value	0.0000	0.0000	0.0000	0.0000	0.0020				
SA 5.0 s	-2.7500	0.7332	-3.3747	0.5232	0.1573	0.2095	0.1735	0.1991	0.3371
SE	0.1654	0.0565	0.1010	0.0320	0.0577				
p-value	0.0000	0.0000	0.0000	0.0000	0.0066				

the soft-soil amplification is always positive and relevant for both PGA, and short period SAs (see Fig. 1c), for which the largest values are recorded. Similarly, Figure S5 in Supplementary Material shows the predicted shaking as a function of moment magnitude at four different epicentral distances ($R_{epi} = 1,\ 5,\ 10,\ 20\ km$). These latter plots clearly highlight the fast observed attenuation already at epicentral distances between 1 and $10\ km$.

Figure 4 (panels a, c, e, g for PGA and panels b, d, f, h for PGV) shows the residual ϵ values with respect to the distance (panels a and b), the between event residuals δB_e with respect to the source parameter (magnitude and depth, panels c-f) and the site-to-site residuals $\delta S2S_s$ with respect to the soil category (panels g and h) for the calibrated GMMs. The ϵ residuals from the calibrated GMMs are approximately zero, on average, within each bin, with respect to the epicentral distance indicating the absence of systematic trends or bias in the GMMs. The δB_e residuals are shown with respect to the magnitudes and depths (Fig. 4c-f), their value are within the range $[-0.4\ 0.4]$, similarly to other Italian GMMs both for tectonic and volcanic environment (Bindi et al. 2011; Lanzano and Luzi 2020). No clear trend with depth can be inferred, partly because most events are concentrated within a narrow range between 2 and $3\ km$; therefore, there is no evidence to support defining different models for different depths. Finally the site-to-site residuals features medians very close to zero for both considered class site, in particular for PGA. Figure S6 in the Supplementary Material, referring to the periods $T = 0.3\ s$ and $1.0\ s$., shows that similar results hold also for SAs.

To test the new GMMs, we also compared the predictions with the observed shaking recorded during the two events which were excluded from the calibration and another large event recently occurred on 13 March 2025 with $M_w\ 4.0$ ($M_d\ 4.6$; see catalogue in Scala 2025). In this sense, the total residuals, estimated subtracting the median estimates from the observed values for both events included and not included in the calibration are shown in Figure S7. The red stars and the red triangles in Figure S7 mark the residuals for the two events excluded from the calibration (for PGA in Figure S7a and PGV in Figure S7c) and for the $M_w\ 4.0$ earthquake (for PGA in Figure S7b and PGV in Figure S7d), respectively. In the same panels, the blue dots represent the same residual for the data used in the calibration. To quantitatively evaluate whether the residuals from the excluded events are consistent with those from the calibration dataset, we compared their empirical cumulative

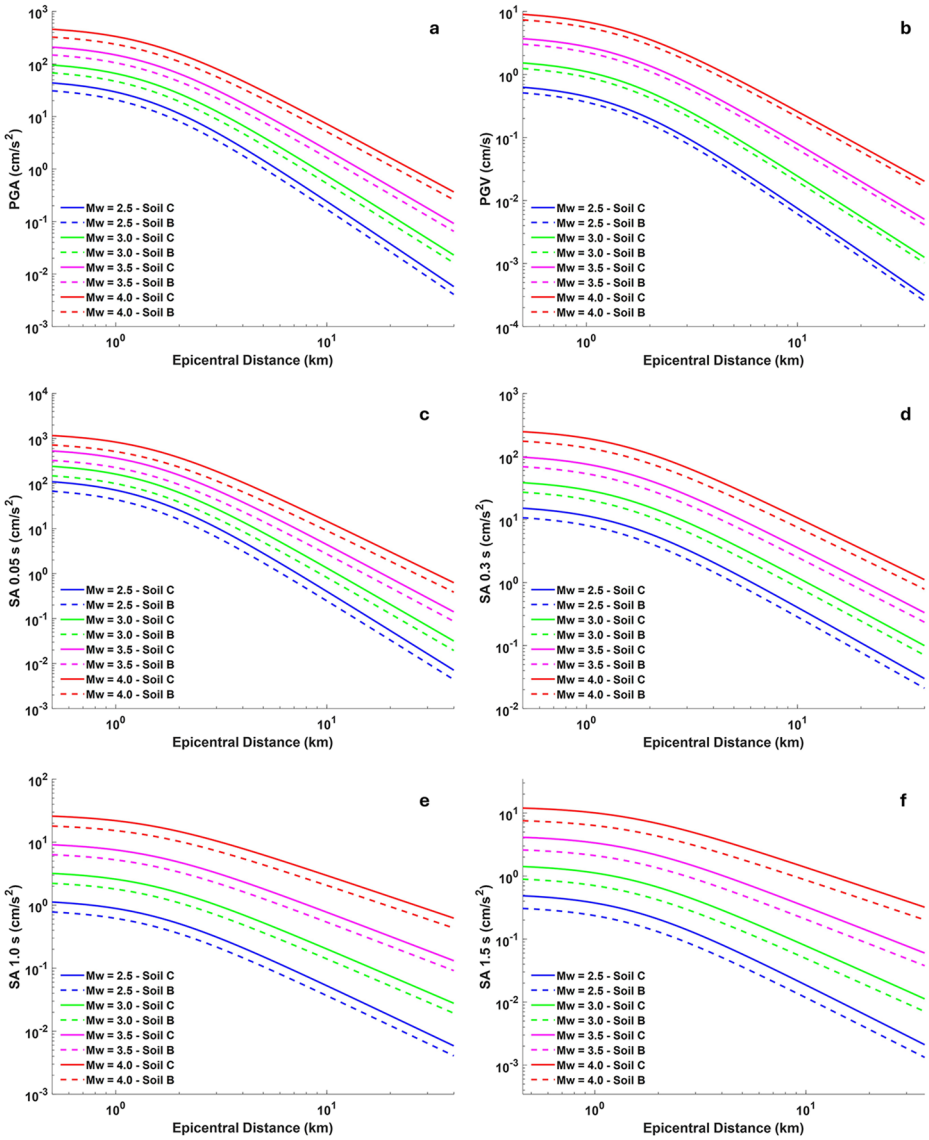

Fig. 3 Ground shaking predicted through the calibrated model (Table 1) as a function of epicentral distance for: (**a**) PGA; (**b**) PGV; (**c**) SA with $T = 0.05\ s$; (**d**) SA with $T = 0.3\ s$; (**e**) SA with $T = 1.0\ s$; (**f**) SA with $T = 1.5\ s$. The models are plotted for four magnitude levels, as indicated in the legend. Solid and dashed lines represent the GMMs for soil C and soil B, respectively

distribution functions (ECDFs). As a statistic test, we used the mean absolute difference between the two ECDFs, which reflects overall differences in the distribution. To assess significance, we employed a bootstrapping approach: subsets of residuals were repeatedly drawn from the calibration dataset, each matching the size of the independent event set, and compared to the full calibration residuals distribution. In this frame, a p-value was defined as the proportion of bootstrap samples yielding a mean absolute ECDF difference greater

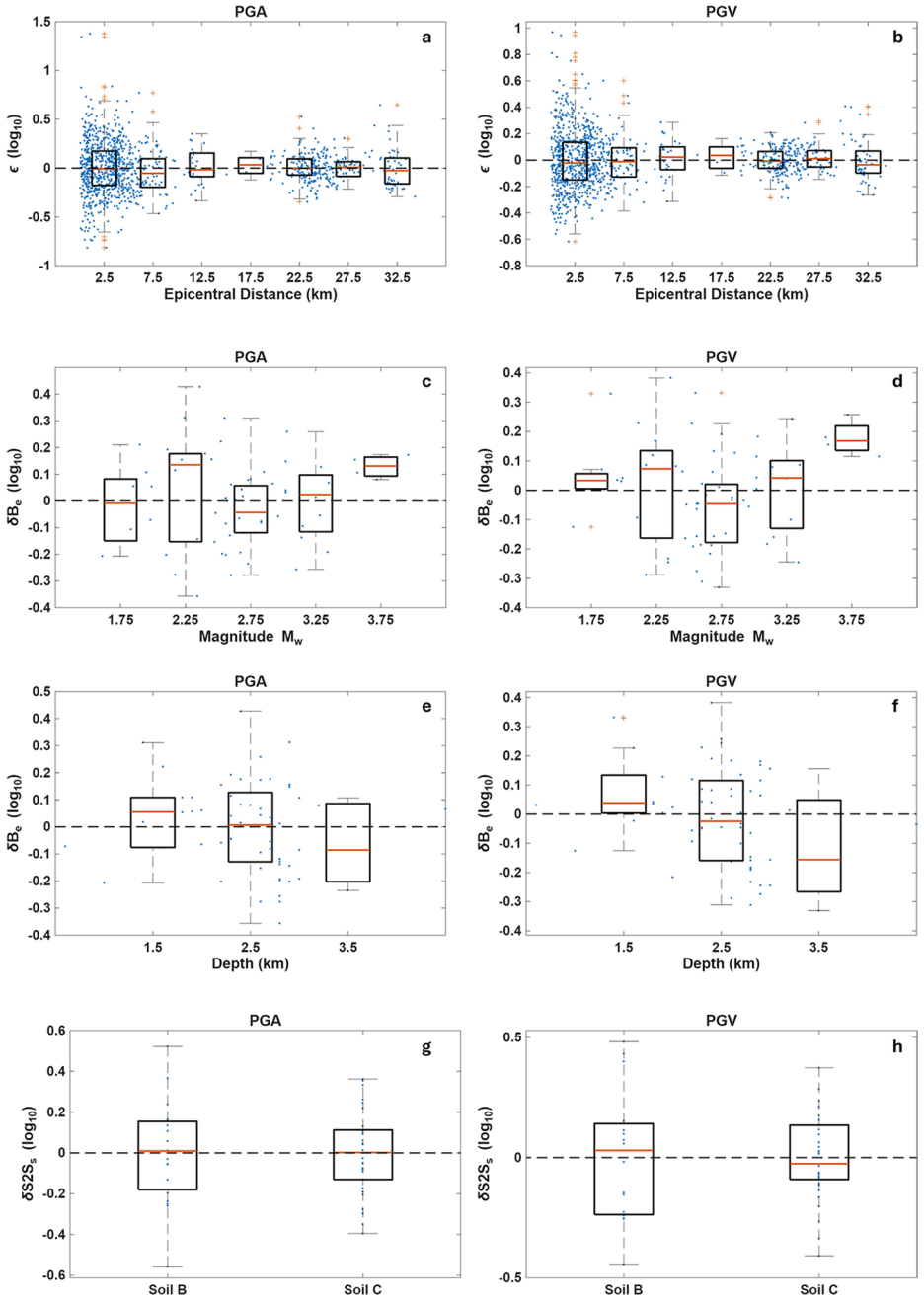

Fig. 4 Residuals (blue dots) and boxplots of observed shaking parameters as compared to the predicted values from the new calibrated models (see Table 1). Within all the boxes the horizontal red lines represent the median, the boxes contain values between 25th and 75th percentiles while the red crosses mark the outliers, that are more than 1.5 times the interquartile range away from the bottom or top of the box. (**a**,**b**) ϵ for PGA and PGV, respectively, as a function of the epicentral distance; (**c**,**d**) $\delta\, B_e$ for PGA and PGV, respectively, as a function of M_w, (**e**,**f**); $\delta\, B_e$ for PGA and PGV, respectively as a function of depth; (**g**-**h**) $\delta\, S2S_s$ for PGA and PGV, respectively as a function of the soil class

than that observed in the actual comparison with the excluded event residuals. For PGA, the resulting p-values in both cases exceeded 0.05, so we did not reject the null hypothesis of distributional similarity at the 95% confidence level. Only for the PGV residuals deriving for the extreme 13 March 2025 event, the p-value is approximately 0.01, leading us to reject the null hypothesis.

3.2 Shaking estimation at Campi Flegrei

The developed model also enables to estimate the shaking that an earthquake produces in the area. Figure 5(a) represents the map of the estimated PGA due to the $M_d = 4.4$ (M_w 4.0) event that occurred on 20th May 2024, while the maps in panel (d) and (g) refer to SA for $T = 0.3\ s$ and $T = 1.0\ s$, respectively. The maps represent the horizontal intensity at more

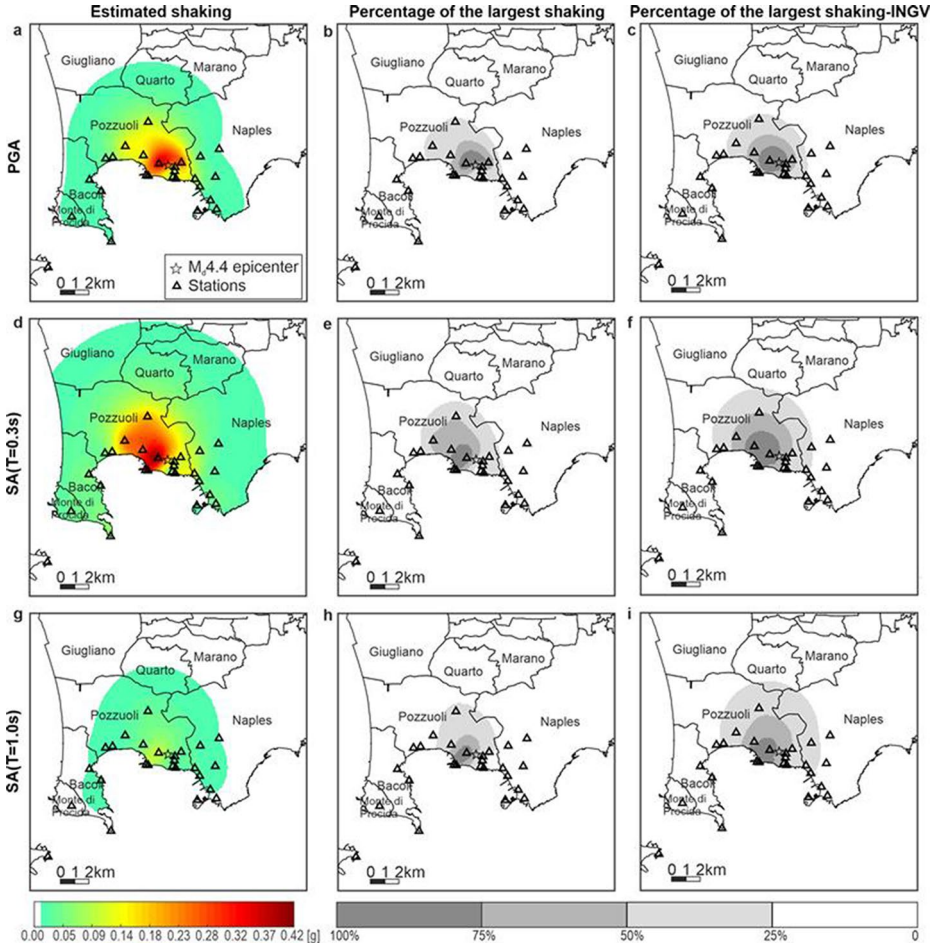

Fig. 5 Estimation of the shaking, on EC8-C local soil site conditions, caused by the $M_d = 4.4$ earthquake occurred on 20 May 2024, in terms of largest horizontal PGA (**a**), SA for $T = 0.3\ s$ (**d**) and $T = 1.0\ s$ (**g**) and map of the shaking normalized by its largest value (**b**,**e**,**h**); panels **c**, **f** and i show the maps based on ShakeMap data, made available by INGV and based on Tusa and Langer (2016) GMMs (only RAN stations are represented in maps from INGV)

than 10,000 sites on a grid, with nodes spaced less than 100 m apart, discretizing the Campi Flegrei inland area. The maps were derived under the assumption that the logarithm of the intensity at the sites follows a multivariate normal (MVN) distribution conditional to earthquake parameters and intensities recorded at the stations, similarly to the approach adopted by ShakeMap (e.g., Worden et al. 2018). The median values of the MVN distribution are the IM values in the maps. These were computed using the GMM presented in this study and modelling the covariance matrix of the MVN distribution using the spatial correlation model for GMM within-event residuals of Esposito and Iervolino (2012), while between-event are considered perfectly correlated (e.g., Giorgio and Iervolino 2016), that is, they have the same value at all the sites in one event. In the analysis, EC8-C class was assumed anywhere, as it is the one attributed to most sites in the area (Forte et al. 2019; Michelini et al. 2019), and stations with epicentral distance within $40\ km$, among those considered by ShakeMap (data are publicly available at https://shakemap.ingv.it/stationList.html?eventid=38759141%26eventyear=2024, last accessed December 2024), were considered to avoid extrapolation of the GMM.

The figure shows that the largest PGA and SA ($T = 0.3\ s$) approach to 0.37 g and 0.42 g, respectively, which are consistent with the values recorded at the station being closest to the event epicentre ($R_{epi} \cong 0.7\ km$). In the case of $T = 1.0\ s$, the largest estimated shaking is about 0.1 g. In Fig. 5(b), sites are represented by shade of grey which varies depending on the interval the estimated PGA, normalized by largest value mapped in Fig. 5(a), belongs to. The shaking in terms of fraction with respect to the maximum value for $T = 0.3\ s$ and $T = 1.0\ s$ is represented in Fig. 5(e) and Fig. 5(h), respectively. It emerges that the attenuation is such that the reduction of the largest SA for $T = 0.3\ s$ is by 25% at epicentral distances lower than $1.8\ km$, and it reduces by 50% already at less than $3.6\ km$ from the epicentre. For the other two considered intensity measures, the largest estimated shaking reduces by 25% [50%] at epicentral distances lower than $1\ km$ [$2\ km$]. For comparison, Fig. 5(c, f, i) shows the maps of the percentage of the largest shaking built on data from ShakeMap (https://shakemap.ingv.it/downloadPage.html?eventid=38759141, last accessed December 2024). For the considered earthquake, ShakeMap provides maps of the estimated shaking using the GMM of Tusa and Langer (2016), coupled with the correlation model of Loth and Baker (2013), referring to local site conditions as provided by large scale geological maps (Michelini et al. 2019), which attribute EC8-C class at most sites. Maps from INGV exhibit comparatively weaker attenuation, especially around the epicentre. The largest estimated intensity for $T = 0.3\ s$ reduces by 25% or less up to $2.5\ km$, and for distances within $1.5\ km$ in the case of PGA and $T = 1.0\ s$. However, at most of the sites outside Pozzuoli, including those in Naples, the largest intensity reduces by more than 75% according to both the maps based on the GMM presented in this study and those from the ShakeMap released by INGV.

4 Discussion

4.1 Additional ground motion model

In the previous section, new GMMs calibration for the Campi Flegrei volcanic region were shown. Such a calibration, valid for the horizontal component of the IMs, makes use of

moment magnitude and epicentral distance as covariates. In this subsection, additional GMMs, possibly useful for practical applications, will be presented, while a broaden discussion about the results, in terms of SAs, aleatory variability and site effects will be the argument of the next subsection.

The coefficients of calibration based on the hypocentral distance and the same functional form of Eq. (5) are collected in Table 2. As previously mentioned, for this regression $h = 1.0\ km$. In Fig. 6, the residuals for PGA and PGV with respect to this model are plotted, similarly to Fig. 4, that is ϵ as a function of hypocentral distance (Fig. 6a and b), δB_e respect to the moment magnitude (Fig. 6c and d), and depth (Fig. 6e and f) and $\delta S2S_s$ as a function of soil class (Fig. 6g and h) are shown. These residuals follow trends similar to those observed for the proposed R_{epi} model. Notably, where hypocentral depth exerts a stronger influence on the model, the δB_e residuals have medians closer to zero across all the bins, further supporting a single-model formulation within the sampled depth range.

As already mentioned, INGV-OV releases the event size in terms of M_d. Therefore, it may be useful to provide a further calibration, based on M_d. Such a calibration, based on the maxima between the two horizontal components, is presented in Table 3. The estimated σ_0 and σ_T obtained for M_d-based GMMs are systematically larger than the ones obtained considering M_w. The differences between the aleatory variability for the two cases are shown in Figure S8 in the Supplementary Material. Such a smaller variability indicates that M_w has a largest explanatory power despite the moment magnitude provided here is sensitive to the earthquake location and the velocity model, especially in the source vicinity (Supino et al. 2024). While location was improved by coupling source-station specific travel-times and amplitudes in the NNLoc-SSST-Coherence algorithm (Lomax & Savvaidis, 2022; Scotto di Uccio et al., 2024), the selection of specific crustal models may result into different magnitude estimations (see Scotto di Uccio et al., 2024; Supino et al. 2024). However, assuming a first-order layered model, this variability mainly results into systematic shifts in the M_w estimates not affecting the calibrated attenuation.

All the results discussed so far pertain to the horizontal component of the shaking, estimated as the largest value between the two components for all the parameters. However, the largest events generated significant vertical motion in the vicinity of the causative source, inducing shaking comparable to that recorded on the horizontal components, this motivating the computation of GMMs for the vertical PGV, PGA and SAs. Although the predicted vertical shaking is generally lower than the horizontal one, as shown for PGA (Fig. 7a, average vertical to horizontal, V/H, ratio ~ 0.78) and for the SAs (Fig. 7b), approximately 17% of the records from events with $M_w \geq 3.5$ and epicentral distances $R_{epi} \leq 10km$ exhibit a $V/H > 1$, with a maximum value of 2.7 (Fig. 7c). This behaviour has been previously documented in Italy both for crustal events (Ramadan et al. 2021) and other volcanic areas (Ramadan et al. 2023). A deeper investigation into the underlying causes, such as site effects, source radiation patterns, or topographic amplification, would be warranted. However, such an analysis lies beyond the scope of the present study. For such a vertical calibration the same functional form used for the horizontal component (Eq. 5), with epicentral distance and moment magnitude as covariates, and $h = 1.4\ km$, was adopted. The coefficients are reported in Table 4.

Table 2 Coefficients of horizontal GMMs calibration (maximum among horizontal components) for PGA, PGV and SAs with the functional form of Eq. (5) and using the hypocentral distance. Parameter h = 1.0 km for all the IMs

Parameters	a	b	c	c_2	e_c	τ	ϕ_{S2S}	σ_0	σ_T
PGA	0.3439	0.9372	-3.7449	0.1718	0.0511	0.1968	0.2787	0.2577	0.4276
SE	0.1862	0.0611	0.1484	0.0484	0.0905				
p-value	0.0651	0.0000	0.0000	0.0004	0.5724				
PGV	-1.7282	0.9950	-3.1904	0.1368	-0.0058	0.1468	0.2484	0.2107	0.3573
SE	0.1481	0.0473	0.1212	0.0395	0.0796				
p-value	0.0000	0.0000	0.0000	0.0005	0.9415				
SA 0.02 s	0.5330	0.9108	-3.9743	0.2321	0.0498	0.2143	0.2846	0.2915	0.4603
SE	0.2034	0.0673	0.1663	0.0545	0.0939				
p-value	0.0089	0.0000	0.0000	0.0000	0.5958				
SA 0.03 s	0.6720	0.9307	-4.1345	0.2363	0.0893	0.2414	0.2974	0.3031	0.4884
SE	0.2205	0.0736	0.1739	0.0569	0.0981				
p-value	0.0024	0.0000	0.0000	0.0000	0.3627				
SA 0.05 s	0.7207	0.9386	-4.1303	0.2377	0.1244	0.2373	0.2707	0.3013	0.4694
SE	0.2153	0.0726	0.1717	0.0564	0.0906				
p-value	0.0008	0.0000	0.0000	0.0000	0.1702				
SA 0.075 s	0.6235	0.9193	-3.8811	0.2224	0.1447	0.2192	0.2515	0.2796	0.4353
SE	0.1993	0.0671	0.1593	0.0523	0.0842				
p-value	0.0018	0.0000	0.0000	0.0000	0.0861				
SA 0.1 s	0.4839	0.9231	-3.4819	0.1392	0.1288	0.2025	0.2637	0.2500	0.4160
SE	0.1855	0.0615	0.1442	0.0470	0.0860				
p-value	0.0092	0.0000	0.0000	0.0031	0.1344				
SA 0.15 s	0.0722	0.9656	-2.8804	0.0359	0.1290	0.1604	0.2535	0.2176	0.3706
SE	0.1566	0.0505	0.1256	0.0409	0.0814				
p-value	0.6450	0.0000	0.0000	0.3793	0.1133				
SA 0.2 s	-0.1001	0.9469	-2.7656	0.0653	0.1051	0.1405	0.2572	0.2025	0.3563
SE	0.1443	0.0454	0.1170	0.0380	0.0816				
p-value	0.4878	0.0000	0.0000	0.0856	0.1979				
SA 0.25 s	-0.3376	1.0018	-2.6452	0.0420	0.0519	0.1416	0.2584	0.1917	0.3515
SE	0.1421	0.0447	0.1116	0.0361	0.0813				
p-value	0.0177	0.0000	0.0000	0.2447	0.5234				
SA 0.3 s	-0.5348	1.0284	-2.5341	0.0283	0.0243	0.1390	0.2622	0.1819	0.3481
SE	0.1390	0.0433	0.1065	0.0343	0.0819				
p-value	0.0001	0.0000	0.0000	0.4098	0.7670				
SA 0.4 s	-0.8112	1.0424	-2.4822	0.0501	-0.0086	0.1312	0.2571	0.1706	0.3353
SE	0.1320	0.0408	0.1002	0.0322	0.0799				
p-value	0.0000	0.0000	0.0000	0.1202	0.9140				
SA 0.5 s	-1.1361	1.0357	-2.3516	0.0753	0.0330	0.1457	0.2410	0.1632	0.3255
SE	0.1351	0.0431	0.0966	0.0310	0.0751				
p-value	0.0000	0.0000	0.0000	0.0152	0.6600				
SA 0.75 s	-1.5799	1.0264	-2.4344	0.1562	0.0586	0.1596	0.2033	0.1652	0.3068
SE	0.1385	0.0460	0.0972	0.0314	0.0648				
p-value	0.0000	0.0000	0.0000	0.0000	0.3661				
SA 1.0 s	-1.8728	1.0248	-2.6233	0.2340	0.0692	0.1749	0.1995	0.1748	0.3177
SE	0.1480	0.0499	0.1025	0.0332	0.0643				
p-value	0.0000	0.0000	0.0000	0.0000	0.2821				
SA 1.5 s	-2.3300	1.0284	-2.8500	0.3045	0.1357	0.1881	0.1785	0.1893	0.3211

Table 2 (continued)

Parameters	a	b	c	c_2	e_c	τ	ϕ_{S2S}	σ_0	σ_T
SE	0.1561	0.0537	0.1095	0.0358	0.0593				
p-value	0.0000	0.0000	0.0000	0.0000	0.0223				
SA 2.0 s	-2.6197	1.0301	-2.9099	0.3235	0.1640	0.1985	0.1725	0.1962	0.3281
SE	0.1625	0.0563	0.1130	0.0370	0.0580				
p-value	0.0000	0.0000	0.0000	0.0000	0.0048				
SA 3.0 s	-2.7296	0.9921	-3.1817	0.3656	0.1408	0.1867	0.1656	0.2035	0.3220
SE	0.1571	0.0543	0.1161	0.0382	0.0565				
p-value	0.0000	0.0000	0.0000	0.0000	0.0128				
SA 4.0 s	-2.7761	0.9643	-3.3290	0.3798	0.1289	0.1748	0.1761	0.2087	0.3242
SE	0.1532	0.0523	0.1188	0.0391	0.0597				
p-value	0.0000	0.0000	0.0000	0.0000	0.0309				
SA 5.0 s	-2.7188	0.9130	-3.5715	0.4415	0.1105	0.1682	0.1843	0.2119	0.3273
SE	0.1514	0.0513	0.1205	0.0396	0.0621				
p-value	0.0000	0.0000	0.0000	0.0000	0.0754				

4.2 Response spectra, aleatory variability and site effects

To broaden the discussion about the SAs, Fig. 8 shows the median acceleration spectra corresponding to the maximum recorded magnitude $(M_w = 4.0)$ at different distances comparing the proposed GMMs with LL16 (panel a) and RLS23 (panel b), respectively. It is noteworthy that at distances $R_{hypo} = 5\ km$ the spectral peak occurs at short periods, more closely to what predicted by crustal GMMs (Lanzano et al. 2019) rather than by volcanic GMMs (Ramadan et al. 2023), as highlighted in the Fig. 8(b), where the spectra from Lanzano et al. (2019) model is also reported for sake of comparison, considering a *Joyner-Boore distance* (Joyner and Boore 1981) $R_{JB} = 5\ km$.

In terms of aleatory variability, the total standard deviations σ_T of the proposed GMMs, for horizontal IM and epicentral distance are shown in Fig. 9(a) for PGA, PGV and SA(T). Comparing σ_T with that from available models, we found smaller variability for PGA and for most of the SAs with respect to TL16. Compared to RLS23, the variability for PGA is slightly larger, while it is significantly smaller in the short period range where the largest shaking is predicted by the GMMs presented in this work.

For what concerns the local site effects due to soil C as compared to soil B, we retrieved systematically larger coefficients for PGA and an increasing trend towards the short period SAs $(T \leq 0.2\ s)$, in contrast to what retrieved in previous models like RLS23 (Fig. 9b). Such an unexpected trend, leading to large C-class amplification at higher frequencies, may indeed be an artifact, related to the very high SA values observed at very short epicentral distances, where most of the recordings correspond to C-class sites (see Fig. 1b). To explore this hypothesis, we analysed the correlation coefficients between the intercept term a and the soil C amplification term e_c across different periods. The results support this interpretation: for SA at periods shorter than $0.2\ s$, the anti-correlation is approximately 0.35–0.40, gradually decreasing to about 0.25 at longer periods. High-resolution local geological studies would be required to unravel this issue and accurately assess the contribution of site conditions to the shaking amplification. For sake of completeness, we highlight that in Fig. 9(b), the amplification due to the soil D with respect to soil B prediction is reported for TL16 model. Indeed, in TL16, the few data recorded on soil C were not included in the calibration.

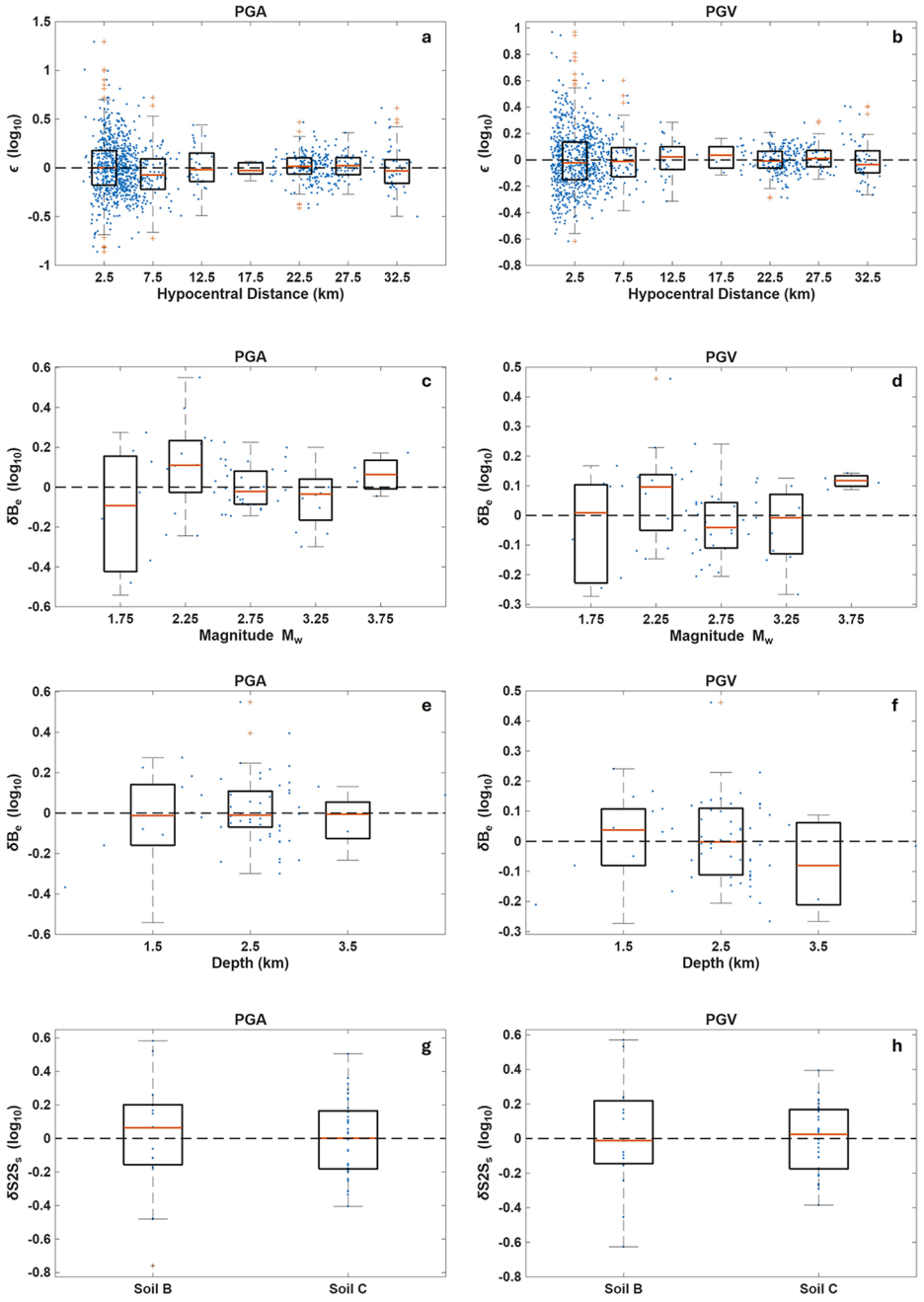

Fig. 6 Residuals (blue dots) and boxplots of observed shaking parameters as compared to the predicted values from GMMs presented in the Table 2 (hypocentral distance as covariate). Within all the boxes the horizontal red lines represent the median, the boxes contain values between 25th and 75th percentiles while the red crosses mark the outliers, that are more than 1.5 times the interquartile range away from the bottom or top of the box. (**a**,**b**) ϵ for PGA and PGV, respectively, as a function of the epicentral distance; (**c**,**d**) $\delta\ B_e$ for PGA and PGV, respectively, as a function of M_w, (**e**,**f**); $\delta\ B_e$ for PGA and PGV, respectively as a function of depth; (**g**-**h**) $\delta\ S2S_s$ for PGA and PGV, respectively as a function of the soil class

Table 3 Coefficients of GMMs calibration, based on duration magnitude M_d, for PGA, PGV and SAs with the functional form of Eq. (5). Parameter h = 1.4 km for all the IMs

Parameters	a	b	c	c_2	e_c	τ	φ	σ_0	σ_T
PGA	0.2109	0.6156	-3.3924	0.2565	0.1412	0.2595	0.2267	0.2530	0.4275
SE	0.2447	0.0757	0.1302	0.0367	0.0750				
p-value	0.3888	0.0000	0.0000	0.0000	0.0601				
PGV	-2.0430	0.7552	-2.8356	0.2019	0.0819	0.2443	0.2161	0.2053	0.3854
SE	0.2242	0.0697	0.1071	0.0298	0.0696				
p-value	0.0000	0.0000	0.0000	0.0000	0.2394				
SA 0.02 s	0.4061	0.5929	-3.5384	0.2818	0.1299	0.2770	0.2303	0.2883	0.4614
SE	0.2639	0.0818	0.1468	0.0417	0.0779				
p-value	0.1242	0.0000	0.0000	0.0000	0.0955				
SA 0.03 s	0.5721	0.5869	-3.6702	0.2884	0.1773	0.2947	0.2444	0.3022	0.4878
SE	0.2799	0.0868	0.1541	0.0437	0.0824				
p-value	0.0412	0.0000	0.0000	0.0000	0.0318				
SA 0.05 s	0.6933	0.5812	-3.7826	0.3178	0.2003	0.2919	0.2344	0.2994	0.4794
SE	0.2766	0.0859	0.1523	0.0433	0.0796				
p-value	0.0123	0.0000	0.0000	0.0000	0.0119				
SA 0.075 s	0.5753	0.5855	-3.6236	0.3215	0.2181	0.2731	0.2302	0.2770	0.4520
SE	0.2590	0.0802	0.1416	0.0401	0.0772				
p-value	0.0266	0.0000	0.0000	0.0000	0.0048				
SA 0.1 s	0.3010	0.6303	-3.1736	0.2333	0.2182	0.2505	0.2432	0.2487	0.4287
SE	0.2392	0.0733	0.1288	0.0361	0.0793				
p-value	0.2085	0.0000	0.0000	0.0000	0.0060				
SA 0.15 s	-0.2887	0.7368	-2.4511	0.0936	0.2276	0.2268	0.2313	0.2183	0.3906
SE	0.2160	0.0660	0.1137	0.0317	0.0744				
p-value	0.1816	0.0000	0.0000	0.0032	0.0023				
SA 0.2 s	-0.5327	0.7521	-2.3063	0.1039	0.2071	0.2216	0.2369	0.2033	0.3828
SE	0.2099	0.0640	0.1067	0.0295	0.0752				
p-value	0.0113	0.0000	0.0000	0.0005	0.0060				
SA 0.25 s	-0.8199	0.8103	-2.1561	0.0793	0.1666	0.2349	0.2412	0.1939	0.3885
SE	0.2174	0.0668	0.1023	0.0282	0.0759				
p-value	0.0002	0.0000	0.0000	0.0050	0.0283				
SA 0.3 s	-1.0524	0.8428	-2.0540	0.0725	0.1482	0.2364	0.2529	0.1847	0.3924
SE	0.2175	0.0668	0.0980	0.0269	0.0786				
p-value	0.0000	0.0000	0.0000	0.0071	0.0597				
SA 0.4 s	-1.3113	0.8550	-2.0443	0.1013	0.1178	0.2484	0.2577	0.1723	0.3972
SE	0.2240	0.0693	0.0920	0.0251	0.0793				
p-value	0.0000	0.0000	0.0000	0.0001	0.1377				
SA 0.5 s	-1.6931	0.8860	-1.9081	0.1076	0.1511	0.2574	0.2590	0.1641	0.4003
SE	0.2291	0.0713	0.0879	0.0240	0.0793				
p-value	0.0000	0.0000	0.0000	0.0000	0.0570				
SA 0.75 s	-2.1378	0.9068	-2.0097	0.1630	0.1503	0.2701	0.2275	0.1642	0.3894
SE	0.2361	0.0745	0.0874	0.0240	0.0706				
p-value	0.0000	0.0000	0.0000	0.0000	0.0335				
SA 1.0 s	-2.4076	0.9101	-2.2138	0.2277	0.1463	0.2859	0.2242	0.1727	0.4023
SE	0.2488	0.0788	0.0916	0.0252	0.0701				
p-value	0.0000	0.0000	0.0000	0.0000	0.0372				
SA 1.5 s	-2.7775	0.9039	-2.5407	0.3066	0.1876	0.3006	0.2074	0.1798	0.4071
SE	0.2597	0.0828	0.0946	0.0262	0.0659				

Table 3 (continued)

Parameters	a	b	c	c_2	e_c	τ	φ	σ_0	σ_T
p-value	0.0000	0.0000	0.0000	0.0000	0.0045				
SA 2.0 s	-3.0828	0.9123	-2.6147	0.3269	0.2131	0.3013	0.2012	0.1859	0.4073
SE	0.2608	0.0832	0.0974	0.0271	0.0646				
p-value	0.0000	0.0000	0.0000	0.0000	0.0010				
SA 3.0 s	-3.1462	0.8632	-2.8777	0.3618	0.1775	0.2915	0.1746	0.1941	0.3913
SE	0.2532	0.0810	0.1002	0.0282	0.0577				
p-value	0.0000	0.0000	0.0000	0.0000	0.0022				
SA 4.0 s	-3.1714	0.8267	-2.9881	0.3664	0.1627	0.2833	0.1719	0.1999	0.3870
SE	0.2480	0.0792	0.1028	0.0290	0.0573				
p-value	0.0000	0.0000	0.0000	0.0000	0.0046				
SA 5.0 s	-3.1195	0.7798	-3.1680	0.4042	0.1413	0.2777	0.1735	0.2040	0.3858
SE	0.2447	0.0779	0.1048	0.0296	0.0580				
p-value	0.0000	0.0000	0.0000	0.0000	0.015				

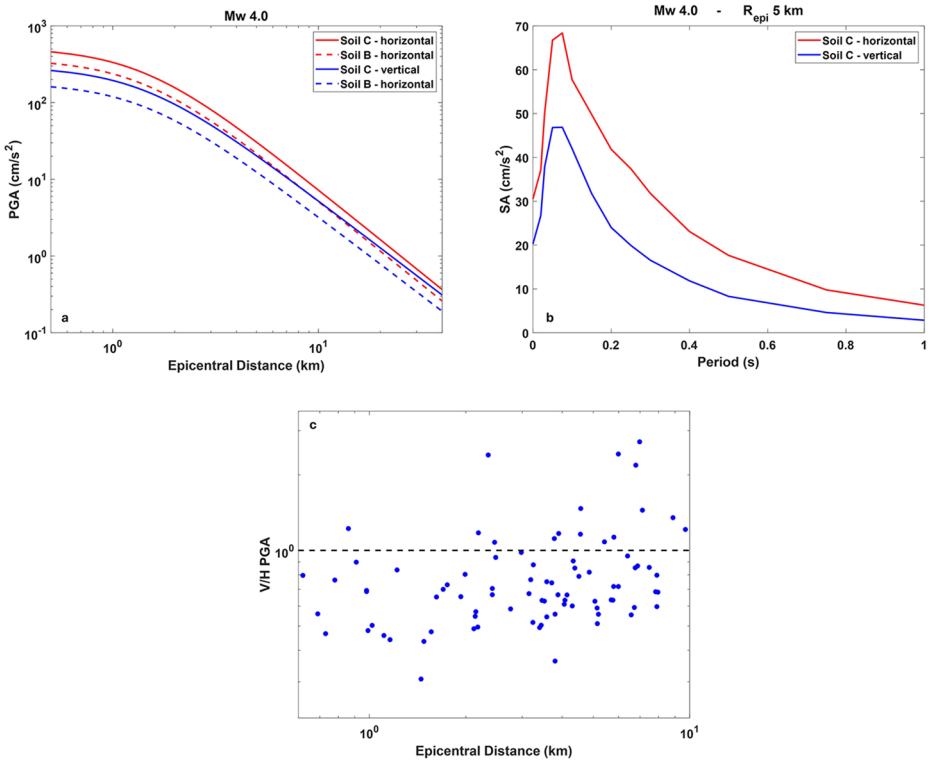

Fig. 7 Results from the vertical GMMs calibration (see coefficients in Table 4). **a)** Comparison between horizontal (red curves) and vertical (blue curves) expected shaking against distance for an event with $M_w = 4.0$. Solid and dashed lines refer to Soil C and Soil B, respectively. **b)** Comparison between expected SAs as a function of the period from horizontal (red curve) and vertical (blue curve) GMMs. Both curves refer to a $M_w = 4.0$ recorded at $R_{epi} = 5\,km$ on a Soil C. **c)** V/H ratio for PGA records considering events with $M_w \geq 3.5$ and data at $R_{epi} \leq 10\,km$

Table 4 Coefficients of vertical GMMs calibration for PGA, PGV and SAs with the functional form of Eq. (5). Parameter h = 1.4 km for all the IMs

Parameters	a	b	c	c_2	e_c	τ	ϕ_{S2S}	σ_0	σ_T
PGA	0.2415	0.5794	-3.5464	0.3749	0.2122	0.1646	0.1989	0.2337	0.3482
SE	0.1514	0.0488	0.1173	0.0372	0.0664				
p-value	0.1110	0.0000	0.0000	0.0000	0.0014				
PGV	-1.8386	0.6528	-3.0266	0.3215	0.1406	0.1662	0.1790	0.1833	0.3054
SE	0.1398	0.0461	0.0935	0.0294	0.0584				
p-value	0.0000	0.0000	0.0000	0.0000	0.0162				
SA 0.02 s	0.4670	0.5782	-3.8257	0.4197	0.1827	0.1794	0.1971	0.2651	0.3759
SE	0.1650	0.0538	0.1315	0.0421	0.0676				
p-value	0.0047	0.0000	0.0000	0.0000	0.0070				
SA 0.03 s	0.6143	0.5943	-3.9691	0.4197	0.2253	0.1933	0.2122	0.2833	0.4033
SE	0.1772	0.0578	0.1406	0.0450	0.0727				
p-value	0.0005	0.0000	0.0000	0.0000	0.0020				
SA 0.05 s	0.6479	0.5775	-3.9207	0.4355	0.2709	0.1832	0.2235	0.2854	0.4062
SE	0.1743	0.0559	0.1419	0.0453	0.0759				
p-value	0.0002	0.0000	0.0000	0.0000	0.0004				
SA 0.075 s	0.5722	0.5597	-3.6976	0.4233	0.2937	0.1818	0.2238	0.2604	0.3885
SE	0.1682	0.0540	0.1307	0.0415	0.0746				
p-value	0.0007	0.0000	0.0000	0.0000	0.0001				
SA 0.1 s	0.2420	0.5908	-3.2136	0.3364	0.3543	0.1777	0.2291	0.2313	0.3709
SE	0.1605	0.0513	0.1176	0.0370	0.0745				
p-value	0.1320	0.0000	0.0000	0.0000	0.0000				
SA 0.15 s	0.0346	0.6173	-2.8290	0.2698	0.2495	0.1651	0.2407	0.2008	0.3543
SE	0.1492	0.0469	0.1036	0.0322	0.0761				
p-value	0.8167	0.0000	0.0000	0.0000	0.0011				
SA 0.2 s	-0.2928	0.6677	-2.5375	0.2250	0.1737	0.1737	0.2447	0.1906	0.3555
SE	0.1517	0.0482	0.0989	0.0307	0.0767				
p-value	0.0538	0.0000	0.0000	0.0000	0.0237				
SA 0.25 s	-0.6128	0.7040	-2.3907	0.2199	0.1774	0.1838	0.2352	0.1783	0.3477
SE	0.1535	0.0497	0.0929	0.0288	0.0735				
p-value	0.0001	0.0000	0.0000	0.0000	0.0159				
SA 0.3 s	-0.8623	0.7366	-2.2612	0.2011	0.1768	0.1965	0.2400	0.1654	0.3515
SE	0.1584	0.0520	0.0868	0.0268	0.0741				
p-value	0.0000	0.0000	0.0000	0.0000	0.0172				
SA 0.4 s	-1.2419	0.7877	-2.1002	0.1754	0.1651	0.2034	0.2206	0.1608	0.3404
SE	0.1596	0.0534	0.0842	0.0260	0.0686				
p-value	0.0000	0.0000	0.0000	0.0000	0.0162				
SA 0.5 s	-1.4493	0.7831	-2.0977	0.1979	0.1701	0.2272	0.2180	0.1529	0.3501
SE	0.1717	0.0586	0.0804	0.0248	0.0675				
p-value	0.0000	0.0000	0.0000	0.0000	0.0119				
SA 0.75 s	-1.9186	0.7987	-2.1055	0.2350	0.2219	0.2473	0.2152	0.1445	0.3583
SE	0.1820	0.0631	0.0762	0.0235	0.0663				
p-value	0.0000	0.0000	0.0000	0.0000	0.0008				
SA 1.0 s	-2.1742	0.7775	-2.348	0.3334	0.2453	0.2526	0.2154	0.1675	0.3718
SE	0.1884	0.0651	0.0876	0.0271	0.0675				
p-value	0.0000	0.0000	0.0000	0.0000	0.0003				
SA 1.5 s	-2.4952	0.7676	-2.6762	0.4172	0.2601	0.2538	0.2108	0.1690	0.3707
SE	0.1890	0.0654	0.0882	0.0274	0.0663				

Table 4 (continued)

Parameters	a	b	c	c_2	e_c	τ	ϕ_{S2S}	σ_0	σ_T
p-value	0.0000	0.0000	0.0000	0.0000	0.0001				
SA 2.0 s	-2.7302	0.7715	-2.8145	0.4525	0.2566	0.2625	0.1942	0.1838	0.3747
SE	0.1950	0.0680	0.0949	0.0297	0.0626				
p-value	0.0000	0.0000	0.0000	0.0000	0.0000				
SA 3.0 s	-2.7890	0.7286	-3.1663	0.5185	0.2088	0.2377	0.1578	0.1873	0.3413
SE	0.1782	0.0624	0.0950	0.0302	0.0528				
p-value	0.0000	0.0000	0.0000	0.0000	0.0001				
SA 4.0 s	-2.7710	0.6839	-3.2989	0.5220	0.1755	0.2191	0.1462	0.1809	0.3196
SE	0.1656	0.0578	0.0914	0.0291	0.0494				
p-value	0.0000	0.0000	0.0000	0.0000	0.0004				
SA 5.0 s	-2.7791	0.6566	-3.3381	0.5095	0.1531	0.2039	0.1446	0.1789	0.3074
SE	0.1564	0.0543	0.0903	0.0288	0.0488				
p-value	0.0000	0.0000	0.0000	0.0000	0.0018				

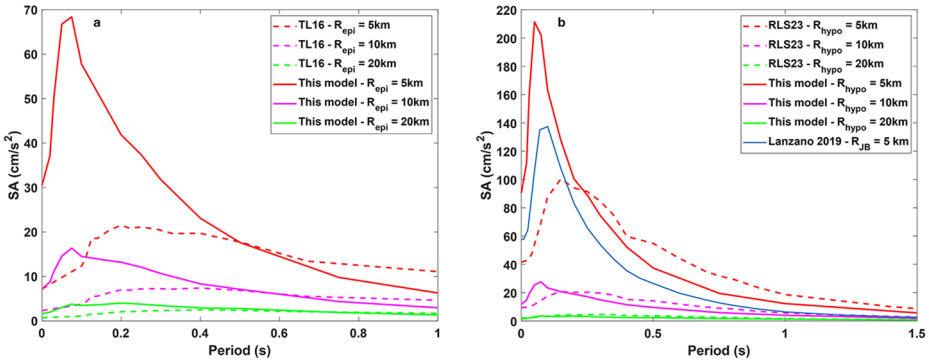

Fig. 8 (**a**) Predicted acceleration spectra for the GMMs calibrated in this work (solid lines, parameters of Table 1) and the TL16 GMMs (dashed lines) at different epicentral distances. (**b**) Predicted pseudo-acceleration spectra for the GMMs calibrated in this work (solid lines, parameters of Table 2) and the RLS23 GMMs (dashed lines) at different hypocentral distances. For sake of comparison the acceleration spectrum for the Lanzano et al. 2019 GMM (crustal event is shown for a Joyner-Boore distance equal to 5 km). All the curves refer to $M_w = 4.0$

5 Conclusions

In this work, we calibrated new GMMs for the Campi Flegrei volcanic region, exploiting the large amount of data recorded during the current unrest of the inner caldera, which is accompanied by a seismic activity, with about seventy events with duration magnitude M_d in the range [2.5,4.4] recorded from March 2022 to May 2024. We verified how some of the state-of-the-art GMMs for Italian volcanic seismicity lead to systematic underprediction of shaking parameters at very short distances $(R_{epi} < 5\ km)$ especially for PGV, PGA and short period SA $(T < 0.2\ s)$. This effect is less significant at intermediate and larger distances $(5\ km < R_{epi} < 40\ km)$ and larger periods $(T > 0.2\ s)$.

Primarily, we moved from the M_d provided by the official bulletin released by INGV-OV to estimations of moment magnitude M_w to homogenise the new calibrated GMMs to

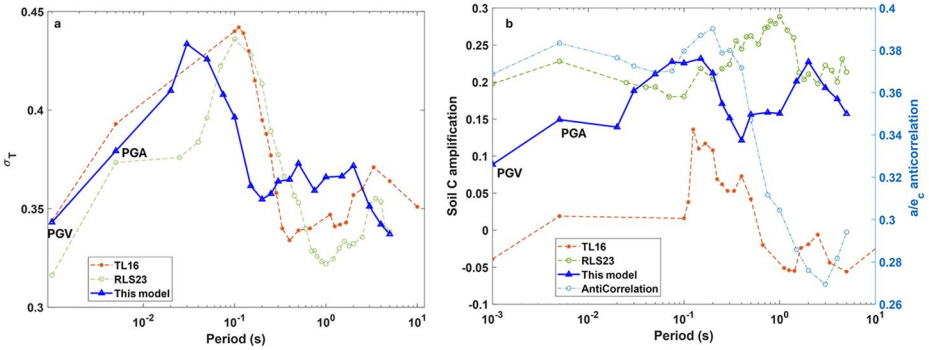

Fig. 9 Comparison of σ_T (panel **a**) and soil C amplification (panel **b**) between the here calibrated GMMs (blue triangles, indicated as "This Model" in the legend, coefficientes presented in Table 1) and the TL16 (orange stars) and RLS23 (green circles) GMMs. In panel (**b**) referred to the vertical right axis the anti-correlation between the parameters a and e_c is shown

the other models already provided for other Italian volcanic regions. For all the parameters, the GMMs based on M_w lead to smaller aleatory variability with respect to the calibration based on M_d.

The best functional form for the new calibrated GMMs was determined through a set of *Bayesian Information Criterion* tests. We finally developed an epicentral-distance-based GMM incorporating a magnitude dependent geometric attenuation and a fixed pseudo-depth $h = 1.4\ km$.

Using the records of the largest events $(M_d > 2.5)$ at the dense permanent seismic network monitoring the region, we calibrated GMMs for PGA, PGV and 5% damped SA at periods T ranging from $0.02\ s$ to $5\ s$, both for the maximum value from the two horizontal components and for the vertical one. For the horizontal shaking, we also provided two further set of GMMs by using either the hypocentral distance or the duration magnitude M_d as covariates.

We showed how the proposed GMMs do not report any bias in residuals distribution with respect to both covariates and depth. They model both the strong shaking at short distance and the observed faster attenuation with distance with respect to other GMMs proposed for Italian volcanic regions and currently used by INGV for ShakeMap implementation. This also emerges from the maps of the estimated shaking due to the $M_d = 4.4$ event that occurred on 20 May, 2024, showing that the largest estimated intensity reduces by 25% at epicentral distances lower than $1.8\ km$ for $T = 0.3\ s$, and $1\ km$ in the case of PGA and $T = 1.0\ s$. Such a reduction, according to counterparts built on ShakeMap data released by INGV, was found at distances within $2.5\ km$ for $T = 0.3\ s$ and $1.5\ km$ for the other two intensity measures. Given that the use of a locally calibrated GMM better captures the peculiarities of the seismicity observed in the area of interest, the proposed model is deemed suitable for seismic hazard and risk analysis studies at Campi Flegrei.

Supplementary Information The online version contains supplementary material available at https://doi.org/10.1007/s10518-025-02315-6.

Acknowledgements We sincerely thank the editor, Giovanni Lanzano and an anonymous reviewer for the valuable comments and feedbacks that have definitely contributed to improve the quality of the work.

Author contributions Antonio Scala, Gaetano Festa, Aldo Zollo, Iunio Iervolino and Vincenzo Convertito contributed to the study conception and design. Material preparation and data collection were performed by Antonio Scala, Antonella Bobbio, Vincenzo Convertito and Luca Elia. Analyses were performed by Antonio Scala (contribution to all the analyses), Claudio Strumia and Francesco Scotto di Uccio (seismic source characterization), Pasquale Cito (shaking map computation) Antonio Giovanni Iaccarino and Antonio Emolo (uncertainty and modelling tests). The first draft of the manuscript was written by Antonio Scala, Claudio Strumia and Pasquale Cito and all authors commented on previous versions of the manuscript. All authors read and approved the final manuscript.

Funding The research has been partially funded by the following projects: Geo-INQUIRE funded by the European Commission under project number 101058518 within the HORIZON-INFRA-2021-SERV-01 call. Go-BEYOND funded by the European Commission under project number 101121135 within the HORIZON-CL3-2022-DRS-01. RETURN funded in the frame of the National Recovery and Resilience Plan (NRRP), Mission 4, Component 2, Investment 1.3 CUP E63C22002000002.

Data availability The data used in this work can be found within the following repository: Scala (2025). Dataset repository for the paper Ground Motion Models Equations for Campi Flegrei (Italy) by Scala et al. [Data set]. In *Zenodo.* https://doi.org/10.5281/zenodo.14591726.

Declarations

Competing interests The authors have no relevant financial or non-financial interests to disclose.

References

Al-Atik L, Abrahamson N, Bommer JJ, Scherbaum F, Cotton F, Kuehn N (2010) The variability of Ground-Motion prediction models and its components. Seismol Res Lett 81(5):794–801. https://doi.org/10.1785/gssrl.81.5.794

Bevilacqua A, De Martino P, Giudicepietro F, Ricciolino P, Patra A, Pitman EB, Bursik M, Voight B, Flandoli F, Macedonio G, Neri A (2022) Data analysis of the unsteadily accelerating GPS and seismic records at Campi flegrei caldera from 2000 to 2020. Sci Rep 12(1):19175. https://doi.org/10.1038/s41598-022-23628-5

Bevilacqua A, Neri A, De Martino P, Giudicepietro F, Macedonio G, Ricciolino P (2024) Accelerating upper crustal deformation and seismicity of Campi flegrei caldera (Italy), during the 2000–2023 unrest. Commun Earth Environ 5(1):742. https://doi.org/10.1038/s43247-024-01865-y

Bindi D, Pacor F, Luzi L, Puglia R, Massa M, Ameri G, Paolucci R (2011) Ground motion prediction equations derived from the Italian strong motion database. Bull Earthq Eng 9(6):1899–1920. https://doi.org/10.1007/s10518-011-9313-z

Boatwright J (1980) A spectral theory for circular seismic sources; simple estimates of source dimension, dynamic stress drop, and radiated seismic energy. Bull Seismol Soc Am 70(1):1–27

Brune JN (1970) Tectonic stress and the spectra of seismic shear waves from earthquakes. J Phys Res 75(26):4997–5009. https://doi.org/10.1029/JB075i026p04997

Calò M, Tramelli A (2018) Anatomy of the Campi flegrei caldera using enhanced seismic tomography models. Sci Rep 8(1):16254. https://doi.org/10.1038/s41598-018-34456-x

Campbell KW, Kuehn NM, Bozorgnia Y (2025) Variability and uncertainty of variance components in fixed-effects and mixed-effects ground-motion models. Earthq Spectra 41(1):731–752. https://doi.org/10.1177/87552930241283717

CEN (2004) Eurocode 8: Design of structures for earthquake resistance.

Chiaraluce L, Valoroso L, Piccinini D, Di Stefano R, De Gori P (2011) The anatomy of the 2009 l'aquila normal fault system (central Italy) imaged by high resolution foreshock and aftershock locations. J Phys Res 116(B12):B12311. https://doi.org/10.1029/2011JB008352

D'Auria L, Giudicepietro F, Aquino I, Borriello G, Del Gaudio C, Lo Bascio D, Martini M, Ricciardi GP, Ricciolino P, Ricco C (2011) Repeated fluid-transfer episodes as a mechanism for the recent dynamics of Campi flegrei caldera (1989–2010). J Phys Res 116(B4):B04313. https://doi.org/10.1029/2010JB007837

Del Gaudio C, Aquino I, Ricciardi GP, Ricco C, Scandone R (2010) Unrest episodes at Campi flegrei: A reconstruction of vertical ground movements during 1905–2009. J Volcanol Geoth Res 195(1):48–56. https://doi.org/10.1016/j.jvolgeores.2010.05.014

De Natale G, Faccioli E, Zollo A (1988) Scaling of peak ground motions from digital recordings of small earthquakes at Campi Flegrei, Southern Italy. Pure Appl Geophys 126(1):37–53. https://doi.org/10.1007/BF00876913

Di Luccio F, Persaud P, Cucci L, Esposito A, Carniel R, Cortés G, Galluzzo D, Clayton RW, Ventura G (2021) The Seismicity of Lipari, Aeolian Islands (Italy) From One-Month Recording of the LIPARI Array. Frontiers in Earth Science 9. https://doi.org/10.3389/feart.2021.678581

Esposito S, Iervolino I (2012) Spatial correlation of spectral acceleration in European data. Bull Seismol Soc Am 102(6):2781–2788. https://doi.org/10.1785/0120120068

Forte G, Chioccarelli E, De Falco M, Cito P, Santo A, Iervolino I (2019) Seismic soil classification of Italy based on surface geology and shear-wave velocity measurements. Soil Dyn Earthq Eng 122:79–93. https://doi.org/10.1016/j.soildyn.2019.04.002

Gaeta FS, Peluso F, Arienzo I, Castagnolo D, De Natale G, Milano G, Albanese C, Mita DG (2003) A physical appraisal of a new aspect of bradyseism: the miniuplifts. J Geophys Research: Solid Earth 108(B8). https://doi.org/10.1029/2002JB001913

Giorgio M, Iervolino I (2016) On multisite probabilistic seismic hazard analysis. Bull Seismol Soc Am 106(3):1223–1234. https://doi.org/10.1785/0120150369

Giudicepietro F, Ricciolino P, Bianco F, Caliro S, Cubellis E, D'Auria L, De Cesare W, De Martino P, Esposito AM, Galluzzo D, Macedonio G, Lo Bascio D, Orazi M, Pappalardo L, Peluso R, Scarpato G, Tramelli A, Chiodini G (2021) Campi Flegrei, vesuvius and Ischia seismicity in the context of the Neapolitan volcanic area. Front Earth Sci 9. https://doi.org/10.3389/feart.2021.662113

Hanks TC, Kanamori H (1979) A moment magnitude scale. J Geophys Research: Solid Earth 84(B5):2348–2350. https://doi.org/10.1029/JB084iB05p02348

Iervolino I, Cito P, De Falco M, Festa G, Herrmann M, Lomax A, Marzocchi W, Santo A, Strumia C, Massaro L, Scala A, di Scotto F, Zollo A (2024) Seismic risk mitigation at Campi flegrei in volcanic unrest. Nat Commun 15(1):10474. https://doi.org/10.1038/s41467-024-55023-1

Joyner WB, Boore DM (1981) Peak horizontal acceleration and velocity from strong-motion records including records from the 1979 imperial valley, California, earthquake. Bull Seismol Soc Am 71(6):2011–2038. https://doi.org/10.1785/BSSA0710062011

Judenherc S, Zollo A (2004) The Bay of Naples (southern Italy): constraints on the volcanic structures inferred from a dense seismic survey. J Geophys Research: Solid Earth 109(B10). https://doi.org/10.1029/2003JB002876

Kanamori H (1977) The energy release in great earthquakes. J Phys Res 82(20):2981–2987. https://doi.org/10.1029/JB082i020p02981

Keir D, De Siena L, Doubre C, Johnson JH, Maccaferri F, Passarelli L (2021) Editorial: Seismicity in Volcanic Areas. Frontiers in Earth Science 9. https://doi.org/10.3389/feart.2021.829460

Kuehn NM, Campbell KW, Bozorgnia Y (2025) Potential biases in Mixed-Effects Ground-Motion models and variance components due to uncertainty in random effects. Bull Seismol Soc Am 115(2):578–601. https://doi.org/10.1785/0120240115

Lanzano G, Luzi L (2020) A ground motion model for volcanic areas in Italy. Bull Earthq Eng 18(1):57–76. https://doi.org/10.1007/s10518-019-00735-9

Lanzano G, Luzi L, Pacor F, Felicetta C, Puglia R, Sgobba S, D'Amico M (2019) A revised Ground-Motion prediction model for shallow crustal earthquakes in Italy. Bull Seismol Soc Am 109(2):525–540. https://doi.org/10.1785/0120180210

Lomax A, Savvaidis A (2022) High-precision earthquake location using source-specific station terms and inter-event waveform similarity. J Geophys Res Solid Earth 127:e2021JB023190. https://doi.org/10.1029/2021JB023190

Loth C, Baker JW (2013) A Spatial cross-correlation model of spectral accelerations at multiple periods. Earthq Eng Struct Dynamics 42(3):397–417. https://doi.org/10.1002/eqe.2212

McGuire RK (2004) Seismic hazard and risk analysis. Earthquake Engineering Research Institute., Ed.), Berkeley

Michele M, Chiaraluce L, Di Stefano R, Waldhauser F (2020) Fine-Scale structure of the 2016–2017 central Italy seismic sequence from data recorded at the Italian National network. J Geophys Research: Solid Earth 125(4). https://doi.org/10.1029/2019JB018440

Michelini A, Faenza L, Lanzano G, Lauciani V, Jozinović D, Puglia R, Luzi L (2019) The new shakemap in italy: progress and advances in the last 10 Yr. Seismol Res Lett 91(1):317–333. https://doi.org/10.1785/0220190130

Peruzza L, Azzaro R, Gee R, D'Amico S, Langer H, Lombardo G, Pace B, Pagani M, Panzera F, Ordaz M, Suarez ML, Tusa G (2017) When probabilistic seismic hazard climbs volcanoes: the Mt. Etna case, Italy – Part 2: computational implementation and first results. Nat Hazards Earth Syst Sci 17(11):1999–2015. https://doi.org/10.5194/nhess-17-1999-2017

Ramadan F, Lanzano G, Sgobba S (2023) Vertical seismic ground shaking in the volcanic areas of italy: prediction equations and PSHA examples. Soil Dyn Earthq Eng 175:108228. https://doi.org/10.1016/j.soildyn.2023.108228

Ramadan F, Smerzini C, Lanzano G, Pacor F (2021) An empirical model for the vertical-to-horizontal spectral ratios for Italy. Earthq Eng Struct Dynamics 50(15):4121–4141. https://doi.org/10.1002/eqe.3548

Ricciolino P, Lo Bascio D, Esposito R (2024) GOSSIP - Database Sismologico Pubblico INGV-Osservatorio Vesuviano. In Istituto Nazionale di Geofisica e Vulcanologia (INGV)

Ricco C, Petrosino S, Aquino I, Cusano P, Madonia P (2021) Tracking the recent dynamics of Mt. Vesuvius from joint investigations of ground deformation, seismicity and geofluid circulation. Sci Rep 11(1):965. https://doi.org/10.1038/s41598-020-79636-w

Scala A (2025) Dataset repository for the paper ground motion models equations for Campi Flegrei (Italy) by Scala [Data set]. In Zenodo. https://doi.org/10.5281/zenodo.14591726

Scarfì L, Aloisi M, Barberi G, Langer H (2023) Observing Etna volcano dynamics through seismic and deformation patterns. Sci Rep 13(1):12951. https://doi.org/10.1038/s41598-023-39639-9

Scotto di Uccio F, Lomax A, Natale J, Muzellec T, Festa G, Nazeri S, Convertito V, Bobbio A, Strumia C, Zollo A (2024) Delineation and fine-scale structure of fault zones activated during the 2014–2024 unrest at the Campi flegrei caldera (Southern Italy) from High-Precision earthquake locations. Geophys Res Lett 51(12). https://doi.org/10.1029/2023GL107680

Selva J, Azzaro R, Taroni M, Tramelli A, Alessio G, Castellano M, Ciuccarelli C, Cubellis E, Lo Bascio D, Porfido S, Ricciolino P, Rovida A (2021) The Seismicity of Ischia Island, Italy: an integrated earthquake catalogue from 8th Century BC to 2019 and its statistical properties. Frontiers in Earth Science 9. https://doi.org/10.3389/feart.2021.629736

Stucchi M, Meletti C, Montaldo V, Crowley H, Calvi GM, Boschi E (2011) Seismic hazard assessment (2003–2009) for the Italian Building code. Bull Seismol Soc Am 101(4):1885–1911. https://doi.org/10.1785/0120100130

Supino M, Festa G, Zollo A (2019) A probabilistic method for the Estimation of earthquake source parameters from spectral inversion: application to the 2016–2017 central Italy seismic sequence. Geophys J Int 218(2):988–1007. https://doi.org/10.1093/gji/ggz206

Supino M, Scognamiglio L, Chiaraluce L, Doglioni C, Herrero A (2024) Source characterization of the 20th May 2024 MD 4.4 Campi flegrei caldera earthquake through a joint source-propagation probabilistic inversion. Seismica 3(2). https://doi.org/10.26443/seismica.v3i2.1394

Tramelli A, Giudicepietro F, Ricciolino P, Chiodini G (2022) The seismicity of Campi flegrei in the contest of an evolving long term unrest. Sci Rep 12(1):2900. https://doi.org/10.1038/s41598-022-06928-8

Tusa G, Langer H (2016) Prediction of ground motion parameters for the volcanic area of Mount Etna. J Seismolog 20(1):1–42. https://doi.org/10.1007/s10950-015-9508-x

Tusa G, Langer H, Azzaro R (2020) Localizing Ground-Motion models in volcanic terranes: shallow events at Mt. Etna, Italy, revisited. Bull Seismol Soc Am 110(6):2843–2861. https://doi.org/10.1785/0120190325

Wald DJ, Quitoriano V, Heaton TH, Kanamori H, Scrivner CW, Worden CB (1999) TriNet shakemaps: rapid generation of peak ground motion and intensity maps for earthquakes in Southern California. Earthq Spectra 15(3):537–555. https://doi.org/10.1193/1.1586057

Wasserstein RL, Lazar NA (2016) The ASA statement on *p* -Values: Context, Process, and purpose. Am Stat 70(2):129–133. https://doi.org/10.1080/00031305.2016.1154108

Worden CB, Thompson EM, Baker JW, Bradley BA, Luco N, Wald DJ (2018) Spatial and spectral interpolation of Ground-Motion intensity measure observations. Bull Seismol Soc Am 108(2):866–875. https://doi.org/10.1785/0120170201

Authors and Affiliations

Antonio Scala[1,3] · Claudio Strumia[1] · Pasquale Cito[2] · Francesco Scotto di Uccio[1] · Gaetano Festa[1,4] · Iunio Iervolino[2,5] · Aldo Zollo[1] · Antonella Bobbio[3] · Vincenzo Convertito[3] · Luca Elia[1,3] · Antonio Emolo[1] · Antonio Giovanni Iaccarino[1]

✉ Antonio Scala
antonio.scala@ingv.it; antonio.scala@unina.it

[1] Dipartimento di Fisica Ettore Pancini, Università degli Studi di Napoli Federico II, Naples, Italy

[2] Dipartimento di Strutture per l'Ingegneria e l'Architettura, Università degli Studi di Napoli Federico II, Naples, Italy

[3] Istituto Nazionale di Geofisica e Vulcanologia (INGV), Sezione Osservatorio Vesuviano, Naples, Italy

[4] Istituto Nazionale di Geofisica e Vulcanologia (INGV), Sezione Osservatorio Nazionale Terremoti, Rome, Italy

[5] IUSS – Scuola Universitaria Superiore di Pavia, Pavia, Italy